fibers

MDPI

Article

Insights on Lattice Discrete Particle Model Calibration and Validation Procedure to Simulate Polypropylene and Steel Fibre-Reinforced Concrete

Sushant Poudel [1], Antonio Cibelli [2], Clementina Del Prete [1], Roman Wan-Wendner [3,*], Claudio Mazzotti [1] and Nicola Buratti [1]

[1] Department of Civil, Chemical, Environmental, and Materials Engineering (DICAM), University of Bologna, 40136 Bologna, Italy; sushant.poudel@studio.unibo.it (S.P.); clementina.delprete@comune.bologna.it (C.D.P.); claudio.mazzotti@unibo.it (C.M.); nicola.buratti@unibo.it (N.B.)
[2] Department of Structures for Engineering and Architecture, University of Naples "Federico II", 80125 Naples, Italy; antonio.cibelli@unina.it
[3] Department of Structural Engineering and Building Materials, Ghent University, 9052 Ghent, Belgium
* Correspondence: roman.wanwendner@ugent.be

Abstract: The use of fibre-reinforced concrete (FRC) has been substantially increasing in the last few years, in different fields of the construction industry. Recently, many experiments have been performed to observe the short- and long-term mechanical behaviour of FRC, and several models have been formulated to capture its mechanical response. In this work, the mechanical behaviour is simulated through the Lattice Discrete Particle Model (LDPM) and its extension to fibre-reinforced cementitious composites (LDPM-F). This paper aims to provide insights into the calibration process and potential pitfalls in a case where only limited experimental data are available—in this case, unconfined uniaxial compression and three-point bending tests on different mixes of polypropylene and steel fibre-reinforced concretes. As a first step, a sensitivity analysis is performed to weight the effect of each governing mesoscale parameter on the simulated macroscale behaviour. Then, for each mix at issue, different sets of model parameters are identified as capable of accurately matching the experimental evidence. As a validation, each calibrated set is used to simulate energy absorption tests on round panels. The validation stage shows that one of the identified sets, for the FRC with polypropylene fibres, accurately matches the round panels' response, while the others result in acceptable predictions. For the mix with steel fibres, instead, none of the sets captures the experimental results, likely due to the different post-cracking behaviour detected in fracture and energy absorption tests. Finally, a parametric study showcases how the LDPM-F might serve as tool to optimise the mix design without extensive experimental investigations.

Keywords: fibre-reinforced concrete; LDPM; LDPM-F; discrete models; lattice models; polypropylene fibre; steel fibre; calibration; validation; sensitivity analysis

check for updates

Academic Editor: Constantin Chalioris

Received: 30 September 2024
Revised: 1 December 2024
Accepted: 26 January 2025
Published: 5 February 2025

Citation: Poudel, S.; Cibelli, A.; Del Prete, C.; Wan-Wendner, R.; Mazzotti, C.; Buratti, N. Insights on Lattice Discrete Particle Model Calibration and Validation Procedure to Simulate Polypropylene and Steel Fibre-Reinforced Concrete. *Fibers* **2025**, *13*, 16. https://doi.org/10.3390/fib13020016

Copyright: © 2025 by the authors. Licensee MDPI, Basel, Switzerland. This article is an open access article distributed under the terms and conditions of the Creative Commons Attribution (CC BY) license (https://creativecommons.org/licenses/by/4.0/).

1. Introduction

The affordability of the raw materials and good mechanical performance in compression make concrete the most used construction materials worldwide. Researchers and professionals, over the years, have improved the design of the mixture composition significantly, enabling the production of concretes featuring compressive strength exceeding 150 MPa. Such cement-based materials are generally referred to as ultra-high-performance concrete (UHPC). However, whereas in compression this material may ensure very high

performance, its mechanical behaviour presents unbeatable weak points, deriving from its own inherent nature. As a matter of fact, concrete features high brittleness, very limited tensile strength, from which derives proneness to the attack of environmental agents due to the unavoidable formation of cracks, and poor impact toughness [1–4].

Since the first engineering applications in which concrete was used to serve as a structural material, the above-mentioned limitations were addressed by either avoiding tensile stresses (i.e., using plain concrete as a surrogate for masonry in pure compression or as prestressed members) or by adopting steel reinforcement bars where tensile stresses are expected to develop. The latter solution is widely referred to as reinforced concrete (RC), and is nowadays the most used construction technology in the civil engineering field. In recent decades, the use of discontinuous reinforcement has been spreading as an alternative technological approach: dispersed short fibres are included in the mixture composition to absorb tensile stresses whenever they are intersected by a fracture. This crack-bridging mechanism and the ensuing improved crack width control result in a substantial improvement in the mechanical response [5,6], with a significant reduction in the stress concentration and a relevant improvement in both material fracture toughness and ductility [7]. On the contrary, the modulus of elasticity and compressive strength are not, or are very slightly, affected by the fibres, which, as shown by many authors, yield, instead, to a less brittle softening branch [8–10].

In fibre-reinforced concrete (FRC), two classes of fibres can be identified, (i) macro- and (ii) micro-fibres, and the two most widely used materials are polymers, mainly polypropylene (PP), and steel, while natural fibres have very limited diffusion [3,11,12]. Depending on the fibre material, the crack width control occurs at either the micro- or macroscale. PP fibres usually work at the microscale, where they limit the crack initiation and development. In addition, PP fibres are naturally hydrophobic and quite efficient in preventing damage due to matrix shrinkage. Furthermore, depending on the fibre volume fraction, they produce significant advantages in corrosion resistance. On the other hand, a drawback is represented by their high creep deformations and sensitivity to temperature variations [13]. Steel fibres, especially those with hooked ends, mainly work at the macroscale, inhibiting the macro-cracks' propagation [14]. In most cases, they provide superior fatigue resistance and post-cracking behaviour if compared to PP fibres [15]. The hooked ends are generally used to increase the fibre–matrix bond and, thus, obtain higher ductility and residual strength than straight fibres [16]. Hooked steel fibres ensure improved performance in terms of crack control [7,17,18]. Recently, a further research development is represented by the use of corrugated or waved fibres. Soulioti et al. [19] proved that specimens with hooked-ended fibres exhibit higher values of toughness and residual strength than specimens with waved fibres, yet the latter seem to ensure higher first-peak strength and peak strength than hooked ones. The debate on which solution, hooked or waved fibres, may represent the best option is still open, as many authors found that linear hooked fibres provide superior overall performance [20,21]. Through dedicated experimental campaigns, many authors proved that polypropylene fibre-reinforced concrete (PPFRC) and steel fibre-reinforced concrete (SFRC) exhibit significant increases in fracture toughness, crack opening control, shrinkage and shear resistance, and durability compared to plain and traditional reinforced concrete [7,15].

In parallel with experimental investigations, over the decades, various numerical models have been proposed to simulate the behaviour of plain and fibre-reinforced concrete at different scales. Two-dimensional (2D) and three-dimensional (3D) miniscale (10^{-4} m or less) models were developed by Wittmann and Carol, respectively, with their coworkers, in which the finite element techniques were used, resulting to be computationally demanding even for small specimens [22–25]. Schlangen and van Mier modelled concrete through

a lattice system and removed the continuum hypothesis used in finite elements [26]. Bolander et al. [27], Yip et al. [28], and Nagai et al. [29] proposed a miniscale discrete model by defining the interactions between polyhedral particles, in which the phenomena occurring at the mesostructural level are responsible for the macroscale mechanical response.

The majority of the numerical approaches for the simulation of the FRC mechanical response rely on macroscopic models combined with fracture mechanics principles (crack, damage, micro-plane models) [30]. Fanella and Krajcinovic [31], Li and Li [32], and Peng and Meyer [33] developed a model based on continuum damage mechanics for the behaviour of concrete under different loading conditions [30]. Xu et al. [34,35] proposed a 2D mesoscale model, while Fang and Zhang [13,36] proposed a 3D mesoscale model to study the failure mechanism of SFRC. Similarly, Han et al. [37] simulated tests on structural components, and were able to capture the unique reverse cyclic loading behaviour of FRC through the development of dedicated constitutive models, whereas Caner et al. [38] introduced the M7f model to realistically capture fibre pull-out and fracture under static and dynamic loading regimes. Finally, Oliver et al. [39] proposed a macroscopic model that accounted for the bond–slip process, happening at the microscale, at the fibre–matrix interface [30].

Among the others, the Lattice Discrete Particle Model (LDPM), as developed by Cusatis et al. [40], demonstrated a superior capability in describing concrete behaviour under a wide range of loading conditions [30,41–43]. In addition, the LDPM was extended to incorporate the effect of fibres (LDPM-F) with remarkable results [44,45]. In [45], Schauffert et al. outlined nine material parameters for the fibre–matrix interaction model and validated the LDPM-F against experimental data, gathered in different laboratory campaigns. Due to the requirement of a plethora of experimental data on the fibre–matrix interaction at the microscale, it is difficult to calibrate all parameters accurately. Many recent studies have explored the utilization of nondestructive techniques in FRC experimental testing to consider the scattering of the fracture energy in the microstructure, which is of great importance for understanding the crack path during the distribution of damage in the fracture surface, and also to address the overlapping of fibres in the microstructure [46,47]. The use of nondestructive evaluation (NDE) techniques provides valuable insights into the fibre–matrix interaction at the microscale and the damage assessment of the FRC. Such data may represent a valuable tool to perform a more accurate calibration when it is not possible to rely on a comprehensive laboratory investigation. However, when only macroscale evidence is available, the model calibration is performed by simulating the structural response (at the macroscale) detected during the tests, and identifying reasonable values for the governing parameters [45].

There are only a few available works in the literature on LDPM-F calibration and validation. Jin et al. [30] performed experimental and numerical simulations of three-point bending tests on steel and polystyrene fibre-reinforced concrete to calibrate LDPM-F parameters. By means of laboratory outcomes gathered through uniaxial unconfined cube compression, three-point bending, and uniaxial strain tests, Smith et al. outlined LDPM-F parameters for an ultra-high-performance concrete with steel fibres [48], whose response to projectile penetration was later simulated [49], after a sound validation against the results relevant to ASTM C39 UC and ASTM modulus of rupture tests [50]. Del Prete et al. [42] calibrated and validated the viscoelastic response of macro-synthetic polypropylene fibre-reinforced concrete through flexural and compression tests. Additionally, Shen et al. [51] studied the mechanical response of SFRC at elevated temperatures, providing the calibrated and validated LDPM-F-HT parameters, using three-point bending and uniaxial compression tests. Finally, Cibelli et al. [52] presented LDPM-F parameters, which were

calibrated and validated for a steel fibre-reinforced concrete by using the evidence collected through three- and four-point bending tests relevant to different ages and specimen sizes.

The aim of this paper is to provide insights into the calibration process of the LDPM-F, showing the potential ambiguity in parameter sets that provide reasonable fits of experimental data, here limited to uniaxial unconfined compression and three-point bending tests. Afterwards, the latter were validated by comparing numerical outcomes and experimental trends in terms of energy absorption of round panels, in order to showcase both the model's potential to predict the behaviour of a structural element and how the predictive capability is heavily affected by the quality of the calibration process. As a matter of fact, a *unique* calibration of the whole parameter set is achievable when extensive experimental investigations are conducted on the material of interest. Data relevant to fracture, tension, uni-, and multiaxial compression tests are needed to identify the parameters governing the plain matrix response, whereas fibre direct tension and single fibre pull-out tests are required to calibrate LDPM-F parameters. When such experimental evidence is missing, the calibration process might be biased and fail in predicting the mechanical response in loading regimes not used for calibration. This aspect is deeply analysed in the following.

Along with the analysis of the calibration process, a comprehensive model sensitivity analysis was realised in order to investigate the effect that each LDPM-F governing parameter has on the simulated macroscale behaviour. Finally, a parametric study was conducted to investigate the effects that the fibres' properties have on the simulated FRC toughness.

In the last decade, LDPM-based models have been developed to allow the simulation of concrete, and cementitious materials on the whole, in a wide range of civil engineering applications. Over the years, particular attention has been paid to enhancing the model's capability of simulating multiphysics problems, where the degradation of concrete is triggered by the contextual occurrence of transport, chemical, and fracture mechanisms. Some examples are (i) behaviour under sustained loads [53], (ii) autogenous crack healing in plain and fibre-reinforced concrete [52,54,55], (iii) damage induced by alkali silica reactions in variable environmental conditions [56,57], (iv) behaviour of ultra-high-performance concrete at an early age [58,59], and (v) chloride diffusion in saturated and non-saturated conditions [60]. The possibility of simulating the responses involved in withstanding such a variety of boundary conditions is particularly appealing nowadays, since it allows us (i) to develop mix compositions tailored to match the scenario-related needs, and (ii) to optimise several activities based on accurate simulations of the multiphysics material response in given environmental conditions, e.g., construction processes in extreme conditions, and water- or fire-proofing for strategical infrastructures. However, such a comprehensive and accurate model simulates the material at the mesoscale, and the path towards the exploitation of the insights resulting from lower-scale modelling at the structural level is paved with computational and theoretical burdens. In [61], a review of the state-of-the-art concepts that allow upscaling of the LDPM is presented. Alternatives for the formulation of computationally efficient macroscale models have been explored in order to leverage both the predictive quality of the LDPM in capturing and predicting the material constitutive behaviour, and the computational affordability that features the classical Finite Element Method for the structural analysis of complex systems.

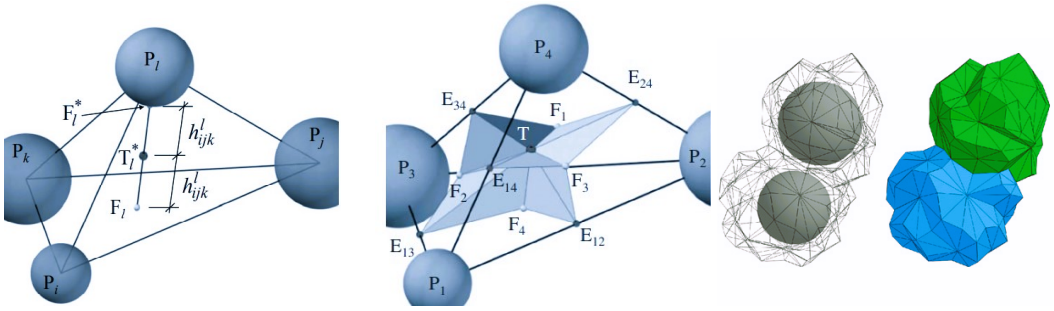
2. Numerical Modelling

2.1. Lattice Discrete Particle Model

The Lattice Discrete Particle Model (LDPM) was formulated to reduce the computational complexity of the miniscale models and accurately capture the fundamental aspects of concrete behaviour. The coalescence of two independent models, (i) the Confinement Shear Lattice (CSL) model [62–64] and (ii) the Discrete Particle Model (DPM) [65], gave rise

to the LDPM, which shares features with both aforementioned models, and presents some unique characteristics.

The LDPM aims to predict the concrete's behaviour, under quasi-static and dynamic loads, through the simulation of the mechanical interactions between polyhedral cells, whose geometry derives from (i) the tetrahedralization of the coarse aggregate centres and the tesselation of the resulting tetrahedron-based mesh. Since the material is simulated as a two-phase material, namely coarse aggregates and an embedding matrix, the model is referred to as a mesoscale model. For a given concrete element, the LDPM mesh is generated as follows: (1) Spherical-shaped particles are randomly introduced and distributed inside the specimen volume, while zero-radius particles are distributed on the external surfaces to therein facilitate the definition of the boundary conditions. (2) TetGen [66] is then used to perform a Delaunay tetrahedralization, which defines a system of tetrahedra with particle centres as vertices (Figure 1a). Each tetrahedron's edge represents an element of the lattice system, simulating the embedding effect that the matrix exerts on the coarse aggregates. (3) Afterwards, the topology of the interaction among the particles is defined through the tessellation of such a tetrahedron-based system into a system of triangular facets (Figure 1b). The result is a system of polyhedral cells that interact through the above-mentioned triangular facets, identified as the locations where the mechanical interaction occurs and the damage is likely to happen (Figure 1c). This last feature is conceived to capture the experimental evidence that for normal-strength concrete, damage and fracture hardly involve aggregates, and generally develop within the embedding matrix.



(**a**) (**b**) (**c**)

Figure 1. (**a**) Definition of arbitrary points (edge, face, and tet points); (**b**) adjacent particles for a typical LDPM tetrahedron tessellation; (**c**) LDPM cells for two adjacent aggregate particles [40].

2.1.1. LDPM Kinematics

In the LDPM, the deformation of the lattice particle system is described by means of rigid body kinematics. Each tetrahedron is divided into four subdomains, each defined by (i) one node (x_i) with displacement component u_i, (ii) a portion of the three tetrahedron edges connected to the node, and (iii) the six triangular tessellation facets connected to the three edges. In each subdomain, the displacement field is defined as follows:

$$u(x) = u_i + \theta_i \times (x - x_i) = A_i(x) Q_i \tag{1}$$

where x_i is the position of the i-th node, and u_i^T and θ_i^T represent the two degrees of freedom, translation, and rotation, respectively, collected into the vector $Q_i^T = [u_i^T \ \theta_i^T]$. The displacement jump at the centroid of the k-th facet, C_k, reads

$$[\![\mathbf{u_{ck}}]\!] = \mathbf{u}_{Cj} - \mathbf{u}_{Ci} \tag{2}$$

in which $\boldsymbol{u}_{Cj} = \boldsymbol{u}(\boldsymbol{x}^{+}_{\boldsymbol{Ck}})$, $\boldsymbol{u}_{Ci} = \boldsymbol{u}(\boldsymbol{x}^{-}_{\boldsymbol{Ck}})$, where i and j refer to the two nodes adjacent to the k-th facet. At the same location, it is possible to define the strain vector along three directions:

$$\varepsilon_N = \frac{\mathbf{n}^T[\![\mathbf{u}_c]\!]}{\ell_e}; \quad \varepsilon_M = \frac{\mathbf{m}^T[\![\mathbf{u}_c]\!]}{\ell_e}; \quad \varepsilon_L = \frac{\mathbf{l}^T[\![\mathbf{u}_c]\!]}{\ell_e} \tag{3}$$

where ℓ_e is the length of the tetrahedron edge, and $\mathbf{n}$, $\mathbf{l}$, and $\mathbf{m}$, are unit vectors defining a local system of reference for each facet. The normal and shear stresses at each facet are calculated through a mesoscale constitutive law expressing σ_k = F(ε_k, ξ_k), where σ_k, ε_k, and ξ_k represent a vector with facet stress, strain, and internal variables. The Principle of Virtual Work (PVW) is then used to impose equilibrium. The discrete equilibrium equations of the LDPM formulation are obtained by summing up the contributions of all the facets and equating the total internal work with the total external work.

2.1.2. LDPM Constitutive Equations

The normal and shear stresses are proportional to the respective strain under the LDPM elastic formulation assumption.

$$\sigma_N = E_N\varepsilon_N; \quad \sigma_M = E_T\varepsilon_M; \quad \sigma_L = E_T\varepsilon_L \tag{4}$$

where $E_N = E_0$ is the normal modulus and $E_T = \alpha E_0$ is the tangential one. E_0 is the effective normal modulus, and α represents the shear–normal coupling parameter. Experimental evidence on the elastic material behaviour is used to calibrate α and E_0. At the mesoscale, the Young's modulus E and Poisson's ratio ν correspond to E_0 and α, and the relationships between them read as follows:

$$E_0 = \frac{1}{1-2\nu}E \longleftrightarrow E = \frac{2+3\alpha}{4+\alpha}E_0 \tag{5a}$$

$$\alpha = \frac{1-4\nu}{1+\nu} \longleftrightarrow \nu = \frac{1-\alpha}{4+\alpha} \tag{5b}$$

In the LDPM, the concrete's response beyond the elastic limit is modelled by considering three different physical mechanisms occurring at the mesoscale: (i) fracturing and cohesive behaviour under tension and shear or their combined action, (ii) high compression causing material compaction and pore collapse, and (iii) frictional behaviour.

When the material is subjected to tensile loading ($\varepsilon > 0$), effective strain and stress allow defining the following relationships in the local reference systems: $\sigma_N = \varepsilon_N(\sigma/\varepsilon)$, $\sigma_L = \alpha\,\varepsilon_L(\sigma/\varepsilon)$, and $\sigma_M = \alpha\,\varepsilon_M(\sigma/\varepsilon)$, in which σ is incrementally elastic ($\dot{\sigma} = E_0\,\dot{\varepsilon}$) and must satisfy the inequality $0 \le \sigma \le \sigma_{bt}(\varepsilon, \omega)$ being $\sigma_{bt}(\varepsilon, \omega)$, a yield surface enforced by means of a vertical (at constant strain) return algorithm. The strain-dependent limit can be expressed as

$$\sigma_{bt}(\varepsilon, \omega) = \sigma_0(\omega)\exp\left[-H_0\,(\omega)\frac{\langle\varepsilon_{max} - \varepsilon_0\rangle}{\sigma_0(\omega)}\right] \tag{6}$$

where the brackets $\langle\cdot\rangle$ are used in the Macaulay sense: $\langle x\rangle = \max\{x, 0\}$, and H_0 is the post-peak softening modulus, whose formulation permits a smooth pass from a softening behaviour under pure tensile stress ($H_0(\omega = \pi/2) = H_t$) to a perfectly plastic response under pure shear ($H_0(0) = 0$). As a matter of fact, $H_0(\omega) = H_t(2\omega/\pi)^{n_t}$, with n_t being the softening exponent. In Equation (6), ω is the parameter representing the degree of interaction between shear and normal loading. Finally, $\sigma_0(\omega)$ is the strength limit for the effective stress and is formulated as

$$\sigma_0(\omega) = \sigma_t\frac{-\sin(\omega) + \sqrt{\sin^2(\omega) + 4\alpha\cos^2(\omega)/r_{st}^2}}{2\alpha\cos^2(\omega)/r_{st}^2} \tag{7}$$

in which $r_{st} = \sigma_s/\sigma_t$ is the ratio between the shear strength, σ_s (cohesion), and the tensile strength, σ_t.

In the presence of a compression load ($\varepsilon_N < 0$), the normal stress at each facet centroid must satisfy the inequality $-\sigma_{bc}(\varepsilon_D, \varepsilon_V) \leq \sigma_N \leq 0$. As for the response under tension and tension/shear, the concrete response is governed by a strain-dependent boundary σ_{bc}, depending on volumetric and deviatoric deformations: ε_V and $\varepsilon_D = \varepsilon_N - \varepsilon_V$, respectively. Determined from the tetrahedron volume variation, the volumetric strain is defined as $\varepsilon_V = (V - V_0)/V_0$, and assumed to be equal for all the facets belonging to the same tetrahedron.

It has been experimentally observed that a concrete specimen, loaded in compression beyond the elastic limit, experiences an earlier collapse of the microscale and mesoscale pores, followed by significant material compaction when the walls of collapsed pores enter into contact. In the LDPM, this phenomenon is modelled through a two-step inelastic evolution of the boundary in compression: σ_{bc} grows linearly during the phase of pore collapse (yielding) up to a threshold value of the compaction strain ($\varepsilon_{DV} = \varepsilon_V + \beta\varepsilon_D$). Then, it follows an exponential evolution to capture the densification effect (rehardening). The formulation reads

$$\sigma_{bc}(\varepsilon_D, \varepsilon_V) = \begin{cases} \sigma_{c0} & \text{for } -\varepsilon_{DV} \leq 0 \\ \sigma_{c0} + \langle -\varepsilon_{DV} - \varepsilon_{c0} \rangle H_c(r_{DV}) & \text{for } 0 \leq -\varepsilon_{DV} \leq \varepsilon_{c1} \\ \sigma_{c1}(r_{DV}) \exp[(-\varepsilon_{DV} - \varepsilon_{c1}) H_c(r_{DV})/\sigma_{c1}(r_{DV})] & \text{otherwise} \end{cases} \tag{8}$$

where σ_{c0} and ε_{c0} are the stress and strain, respectively, at the onset of pore collapse, r_{DV} is the deviatoric-to-volumetric strain ratio $\varepsilon_D/\varepsilon_V$, and $H_c(r_{DV})$ the initial hardening modulus. Finally, σ_{c1} and ε_{c1} are the stress and strain when rehardening begins.

In the model, within the boundaries identified in the inequality $-\sigma_{bc}(\varepsilon_D, \varepsilon_V) \leq \sigma_N \leq 0$, the normal stress is assumed to be incrementally elastic: $\dot{\sigma}_N = E_{Nc}\dot{\varepsilon}_N$. In order to describe the increased stiffness during unloading, E_{Nc} is defined as

$$E_{Nc} = \begin{cases} E_0 & \text{for } -\sigma_N < \sigma_{c0} \\ E_d & \text{otherwise} \end{cases} \tag{9}$$

where E_d is the densified normal modulus.

In the presence of compressive stresses, the shear strength increases due to frictional effects. This phenomenon is modelled through classical incremental plasticity: incremental shear stresses can be calculated as $\dot{\sigma}_L = E_T(\dot{\varepsilon}_L - \dot{\varepsilon}_L^P)$, and $\dot{\sigma}_M = E_T(\dot{\varepsilon}_M - \dot{\varepsilon}_M^P)$, where the plastic strain increments are assumed to obey the normality rule, namely $\dot{\varepsilon}_L = \dot{\lambda}\partial\varphi/\partial\sigma_L$ and $\dot{\varepsilon}_M = \dot{\lambda}\partial\varphi/\partial\sigma_M$. Here, the plastic potential is expressed as $\varphi = (\sigma_L^2 + \sigma_M^2)^{1/2} - \sigma_{bs}(\sigma_N)$, in which the functional relationship between shear strength and acting compressive stress is captured by the boundary:

$$\sigma_{bs}(\sigma_N) = \sigma_s + (\mu_0 - \mu_\infty)\,\sigma_{N0}\,\mu_\infty\,\sigma_N - (\mu_0 - \mu_\infty)\,\sigma_{N0}\exp(\sigma_N/\sigma_{N0}) \tag{10}$$

where σ_s is the cohesion, μ_0 and μ_∞ are the initial and final internal friction coefficients, and σ_{N0} is the normal stress at which the transition from μ_0 to μ_∞ happens. Finally, the loading–unloading conditions are expressed by means of the classical Khun–Tucker's conditions: $\varphi\dot{\lambda} \leq 0$ and $\dot{\lambda} \geq 0$.

For a detailed presentation of the LDPM's constitutive laws, the interested reader can refer to the work published by Cusatis et al. in 2011 [40].

2.2. Lattice Discrete Particle Model for Fibre-Reinforced Concrete

The Lattice Discrete Particle Model for fibre-reinforced concrete, hereinafter referred to as the LDPM-F, is an extended version of the LDPM, in which the effect of the fibres on the concrete behaviour is introduced.

At a facet under tension, the mesoscale crack opening, starting to occur when the strain reaches the tensile elastic limit, is expressed by the vector $\boldsymbol{w_c} = w_N\boldsymbol{n} + w_L\boldsymbol{l} + w_M\boldsymbol{m}$, where $w_N = l\,(\varepsilon_N - \sigma_N/E_N)$ is the opening/closure of the crack along the direction orthogonal to the facet, while $w_L = l\,(\varepsilon_L - \sigma_L/E_T)$ and $w_M = l\,(\varepsilon_M - \sigma_M/E_T)$ are two sliding components, catching shear displacements at crack surfaces.

The geometry of each individual fibre is characterised by the diameter d_f (cross-section $A_f = \pi d_f^2/4$) and length L_f. For a given total fibre volume fraction V_f, the number of fibres N_f contained in a specimen volume (V_{sp}) is determined by $N_f = \lceil (V_{sp}V_f)/(A_fL_f) \rceil$, where $\lceil \cdot \rceil$ indicates the ceiling function, which maps to the least integer greater than or equal to $(V_{sp}V_f)/(A_fL_f)$.

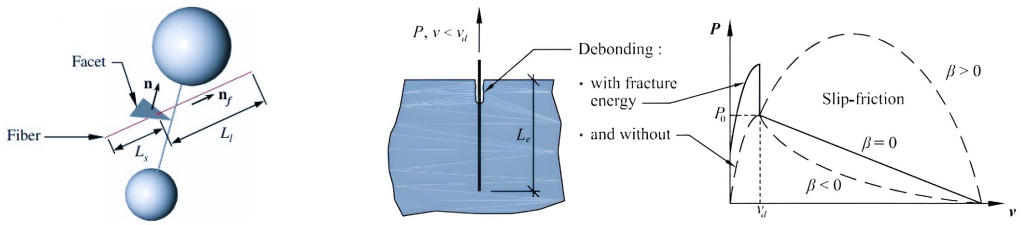
The fibres are added to the LDPM mesh as discrete entities, randomly dispersed within the volume depending on the fibre volume content V_f, and overlapping with the interacting polyhedral cell system. Each facet is associated with the intersecting fibres (Figure 2a), then the crack-bridging phenomenon is implemented at the mesoscale as follows:

$$\sigma = \sigma_c + \frac{1}{A_c}\sum_{f \epsilon A_c} \boldsymbol{P}_f \tag{11}$$

where A_c is the facet area and and $\boldsymbol{P}_f$ represents the crack-bridging force for each fibre crossing the given facet.

During both elastic and inelastic compression regimes, the fibre contribution is assumed to be negligible, while it does contribute to the equilibrium within inelastic tension and shear responses, when the cracking process on the facet initiates.

Since all the mechanisms governing the fibre–matrix interaction develop at a scale which is typically smaller than that one of coarse aggregates—namely, the observation scale adopted for all LDPM formulations—they are not explicitly modelled at the mesoscale. They are taken into account within the formulation of the bridging force P_f.



(**a**) (**b**)

Figure 2. (**a**) Fibre intersecting with LDPM facet; (**b**) fibre debonding and the relationship between load and slippage [44].

2.3. Constitutive Equations for Fibre–Matrix Interaction

A fibre must be completely debonded from the concrete matrix to trigger the purely frictional pull-out between the matrix and fibre. The fibre pull-out is a combination of two phenomena (Figure 2b): (i) initiation and propagation of the interface crack, also referred to as the *tunnel crack*, which is governed by the bond fracture energy (G_d), and (ii) friction between the fibre and surrounding matrix, governed by the frictional stress (τ_0) for the portion of the embedded fibre that has debonded. As is shown in Figure 2b, for the

simulation of the post-debonding stage in the bridging force–slip relationship, an additional parameter (β) is used to capture whether the softening branch evolves linearly, or more or less than linearly.

For a general fibre, with modulus of elasticity E_f and embedded length L_e, the critical value of the slip at full debonding [67] v_d is

$$v_d = \frac{2\,\tau_0\,L_e^2}{E_f\,d_f} + \left(\frac{8\,G_d\,L_e^2}{E_f\,d_f}\right)^{1/2} \tag{12}$$

The fibre load during the debonding stage [67] ($v < v_d$) is

$$P(v) = \left[\frac{\pi^2\,E_f d_f^3}{2}(\tau_0 v + G_d)\right] \tag{13}$$

After full debonding [67], $P(v)$ fully relies on the pure frictional resistance and reads

$$P(v) = P_0\left(1 - \frac{v - v_d}{L_e}\right)\left[1 + \frac{\beta(v - v_d)}{d_f}\right] \tag{14}$$

where $P_0 = \pi L_e d_f \tau_0$ is the initial pull-out force, whereas β [68] is a dimensionless quantity ($\beta > 0$ for slip hardening, $\beta < 0$ for slip softening, and $\beta = 0$ if slip distance is independent of interfacial friction).

The most significant mechanisms, governing the fibre–matrix interaction at the microscale, are taken into account within the calculation of the fibre load. At the point where the fibre exits the matrix and changes orientation, bearing stresses appear in the underlying matrix. When this localised stress field reaches a sufficiently large intensity, spalling occurs. In the LDPM-F, the matrix spalling is modelled through the reduction in the embedded length of the fibre by the quantity s_f, calculated as follows [69]:

$$s_f = \frac{P_{fN} sin(\theta/2)}{k_{sp}\sigma_t d_f cos^2(\theta/2)} \tag{15}$$

where P_{fN} is the normal component of the total fibre force, $\theta = arccos(\boldsymbol{n}_f^T \boldsymbol{n})$ represents the angle between the embedded fibre direction ($\boldsymbol{n}_f$) and the facet's normal orientation ($\boldsymbol{n}$), σ_t is the mesoscale tensile strength of the matrix, and k_{sp} is a dimensionless material parameter to calibrate against experimental data.

Where the fibre exits the tunnel crack, which is shortened because of spalling, it bends around the intact matrix. Consequently, at the exit point, additional friction and bearing forces lead to a load along the bridging segment larger than that one acting on the embedded portion. This phenomenon is generally referred to as the *snubbing effect*, modelled through the frictional pulley idealization [70], which complies with the fibre pull-out model adopted in the LDPM-F [69]. In order to account for the snubbing effect, the fibre load is enlarged as follows:

$$P_f = exp(k_{sn}\varphi'_f)P(v) \tag{16}$$

where P is defined in Equations (13) and (14), k_{sn} is a dimensionless material parameter to calibrate, and φ'_f is the angle between the fibre inside the matrix and the same fibre deflected after spalling.

The well-known Cook–Gordon effect is accounted for through the parameter k_{cg}. Cook and Gordon predicted that a matrix crack approaching an isolated fibre can cause interface debonding before the crack tip reaches the fibre–matrix interface, if the interfacial strength

is adequately weak [71]. This phenomenon, referred to as the Cook–Gordon effect, implies an additional fibre slippage. In the LDPM-F, the above-mentioned additional slippage is referred to as v_{cg}. This process creates an increment in the crack opening, and the value of v_{cg} is estimated as

$$v_{cg} = \frac{4\,k_{cg}\,P_f}{\pi\,d_f^2\,E_f} \tag{17}$$

where P_f is the fibre bridging force and k_{cg} is the Cook–Gordon parameter, to calibrate against experimental evidence, which can be achieved through in situ SEM analyses [72].

Finally, the fibre load must comply with the rupture strength of the fibre; then, the following relationship must always hold:

$$\sigma_f = \frac{4\,P_f}{\pi\,d_f^2} \leq \sigma_{u.f}\exp(-k_{rup}\,\varphi'_f) \tag{18}$$

in which k_{rup} is a material parameter, and $\sigma_{u.f}$ the ultimate tensile strength of the fibre. In case of fibre stress exceeding the corrected value of strength, P_f is set to zero. The exponential term in Equation (18) reflects experimental evidence showing lower rupture loads in single fibre pull-out tests for increasing values of φ'_f [73].

For a generic fibre, with embedment segment orientation $\boldsymbol{n}_f$, subject to pull-out from both embedment depths due to a crack opening w, and with a spalling length s_f on both sides, the crack-bridging force is given by

$$P_f = P_f\,\boldsymbol{n'_f} \tag{19}$$

with the crack-bridging segment computed as

$$||\boldsymbol{w'}|| = 2s_f + v_s + v_l \tag{20}$$

and

$$||\boldsymbol{n'}|| = \frac{\boldsymbol{w'}}{||\boldsymbol{w'}||} \tag{21}$$

where $||\boldsymbol{w'}||$ is the vector length. The embedment segments consist of a short side (L_s) and a long side (L_l) with the relative slippage v_s and v_l, respectively.

The pull-out resisting forces must be the same on each side:

$$P_f = P(v_s)\exp\left(k_{sn}\varphi'_f\right) = P(v_l)\exp\left(k_{sn}\varphi'_f\right) \tag{22}$$

From the equality in Equation (22), the relative slips v_s and v_l can be computed by an interactive procedure in which the compatibility between the bridging segment and the slips (Equation (20)) is enforced. The crack-bridging problem in Equation (22) is non-linear for two main reasons: (1) the functional link between the spalling length and fibre force, and (2) the non-linearity of the force vs. slip relationship. As a consequence, the problem of computing the fibre force for a given mesoscale crack opening is highly non-linear and needs to be solved iteratively. The following procedure based on two nested iteration schemes is adopted. (1) Begin with the last calculated value of fibre-bridging force, P_f. (2) Compute the spalling length s_f (Equation (15)) and then the current effective embedment lengths. (3) Compute length $||\boldsymbol{w'}||$ and orientation $\boldsymbol{n'}_f$ of the crack-bridging segment. (4) Satisfy the compatibility by setting $v_s = x(||\boldsymbol{w'}|| - 2s_f)$ and $v_l = (1-x)(||\boldsymbol{w'}|| - 2s_f)$, and then iteratively solving for x using $P_s(x) - P_l(x) = 0$. This non-linear equation is solved in this study by using Brent's method [74]. (5) Compute either P_s or P_l, compute a new P_f value with Equation (22), and check for convergence. If the convergence criterion is

met, exit the iteration loop. Otherwise, return to Step 2 with the new value of P_f. (6) Finally, upon convergence, the obtained bridging force is compared with the apparent fibre strength $\sigma_{u.f}$ to check for rupture. The algorithm is robust and, typically, converges with less than 10 iterations.

The model allows the distribution of the fibres within the domain with a preferential orientation. This is accomplished by indicating the percentage of fibres oriented along the desired direction. The placing procedure, then, is carried out accordingly.

Further details on the constitutive relations of fibres and matrix–fibre interaction as well as on the calibration of the governing parameters can be found in [44,45].

3. Experimental Campaign

In order to calibrate the LDPM-F parameters and then validate the process, results from a previous experimental campaign were considered [75]. In particular, three different types of specimens were used: (i) 150 mm × 150 mm x 600 mm prisms, (ii) ϕ 800 mm × 75 mm Round Determinate Panels (RDPs), and (iii) 150 mm cubes. In the reference experimental campaign, the experimental specimens were reinforced using 30 kg/m^3 of steel (S) fibres or 5 kg/m^3 of macro polymeric (P) fibres, respectively. All the samples considered in this work were realised through traditional casting, hence the fibres were dispersed without an intended preferential direction. The nominal properties of the fibres are detailed in Table 1, and the investigated mixes are provided in Table 2.

The specimen naming scheme adopted in this study is structured as follows: [concrete mix]-[batch]-[specimen type][specimen number]. As an example, I-P5-3-RC2 refers to the cast RDP 2 produced from batch 3 of the concrete mix I-P5. Prior to being tested, a 25 mm deep notch was introduced at the bottom of the prismatic samples with a 4 mm wide wet blade saw at an age of 25 days. It is worth noticing that the two different experimental tests involve different crack openings. In three-point bending tests, the maximum detected crack opening is about 3.4 mm, while in RDP tests, the maximum crack opening is about 14 mm.

Table 1. Properties of the fibres.

Material	Code	Length mm	Diameter mm	E_m GPa	T_s MPa	Density g/cm^3
Polypropylene	P	55	0.91	3.9	560	1.0
Steel	S	35	0.55	200	1100	7.8

Table 2. Composition of the investigated concrete mixes. C: Cement CEM II 42.5 R, A: aggregates, SF: Silica Fume, W: water, SP: Superplasticizer, SR: Set Retardant.

Mix	C kg/m^3	A kg/m^3	W l/m^3	W/C -	Fibre Type	Dosage kg/m^3	SP l/m^3	SR l/m^3
I-P5	450	1589	204	0.45	P	5.0	6.1	1.3
I-S30	450	1594	204	0.45	S	30.0	6.1	1.3

Three-point bending tests were used to investigate the flexural behaviour of prismatic specimens, whereas the round panels underwent energy absorption tests. In addition, cubes were used to measure the material's compressive strength. The tests were performed in compliance with the Standards EN-14651 and ASTM C1550-12, respectively. The experimental scatter in the following refers to (i) four uniaxial and three-point bending tests on cubes and prisms, and (ii) three energy absorption tests, for each mix of interest. During the three-point bending test, a 50 kN load cell measured the force applied, while the crack mouth opening displacement (CMOD) was measured through dedicated transducers. The

flexural tests were carried out under closed-loop CMOD control, with a crack opening rate of 0.05 mm/min up to CMOD = 0.1 mm, raised to 0.2 mm/min afterwards.

The nominal stress in the notched section was determined by employing Formula (A.2) of the Standards [76], which reads

$$f_{ct.fl} = \frac{3\,F\,l}{2\,d_1\,d_2^2} \tag{23}$$

where F is the applied load, l is the distance between the bottom pin supports, and d_1 and d_2 are, respectively, the width and height of the notched cross-section.

During energy absorption tests, a 50 mm stroke LVDT transducer was used to measure the deflection at the centre of the panel, and three 10 mm stroke LVDTs tracked the support displacements. Additionally, the crack openings perpendicular to the principal crack directions were recorded by means of three potentiometers. As prescribed by the ASTM C1550-12 guidelines, the tests were carried out in displacement control with a displacement rate of 4 mm/min.

The interested reader can find a detailed description of the tests and results in [75], and in Table 3, the average peak force detected on prismatic specimens and the average energy absorption capacity of RDPs are reported.

Table 3. Number of specimens, peak force for prisms, and energy absorption capacity for RDPs.

Mix	**Prism (P)**	**F_{max} kN**	**RDP**	**E J**
I-P5	4	19.0	3	252
I-S30	4	26.3	3	312

4. Sensitivity Analysis

In the LDPM and LDPM-F, the formulation of fibre-reinforced concrete behaviour relies on (i) 17 parameters, governing the response of the plain matrix, and (ii) 10 parameters, controlling the simulation of the fibres' response and their interaction with the embedding matrix. Physical, mechanical, and geometrical parameters of fibres (such as length, strength, dosage, etc.) are not considered here since in many cases, they are known and, therefore, are excluded from model calibration. However, their effect will be analysed in the parametric study presented in Section 6.

To fully calibrate the model, several tests are required. In Table 4, all the LDPM and LDPM-F governing parameters are reported, with the indication of the laboratory test required for a proper calibration of the mesoscale parameters such that good agreement between the simulated response at the macroscale (virtual test) and the experimental evidence (actual test) is reached. Uniaxial (unconfined), bi/triaxial compression, and fracture (three- or four-point bending) tests represent the minimum set of laboratory investigations on the plain matrix to fully calibrate the LDPM governing parameters. In many applications, confined compression stress states are less of a concern, and the need to calibrate several of the parameters is removed. In the presence of fibres, single fibre pull-out tests, with different embedment lengths and fibre orientation, enable the identification of the parameters that govern the fibre–matrix interaction. Along with them, fibre direct tension tests are ideally necessary to characterise (i) the fibre's Young's modulus and (ii) tensile strength, both usually also provided by the producer, (iii) post-elastic behaviour (γ_p, relevant for ductile materials such as steel), and, finally, (iv) the strength decay which the fibre might experience because of its bending at the point where it exits the matrix [44].

Table 4. Models parameters.

Model	Parameters	Calibration Test
LDPM	E_0, σ_t, l_t, n_t	fracture
	α	compression or tension
	μ_0, μ_∞, σ_{N0}	triaxial compression
	σ_{c0}, κ_{c0}, κ_{c1}, κ_{c2}, E_d/E_0	compression
	r_{st}	compression and fracture
	k_t, k_s, k_c	cyclic loads
LDPM-F	E_f, σ_{uf}, k_{rup}, γ_p	fibre direct tension
	τ, β, G_d, k_{sn}, k_{sp}, k_{cg}	single fibre pull-out

Since it may happen that such an extensive experimental database is not available for the material of interest, some of the parameters listed in Table 4 can be assumed by relying on relevant published works. However, the analysis of model sensitivities to the variation of each governing parameter might still be a useful part of the calibration process [77]. In the following, the sensitivity analysis is focused on those parameters which affect (i) the material's response to fracture and uniaxial compression tests (E_0, σ_t, l_t, n_t, r_{st}, μ_0) and (ii) the fibre–matrix interaction (τ, k_{cg}, G_d, β, k_{sn}, k_{sp}). Uniaxial compression and three-point bending tests have been simulated by using the parameters reported in Table 5 as a starting point. Then, the LDPM and LDPM-F parameters of interest were varied within the given intervals in order to visualise the changes that each of them produces on the simulated macroscale behaviour in compression and bending.

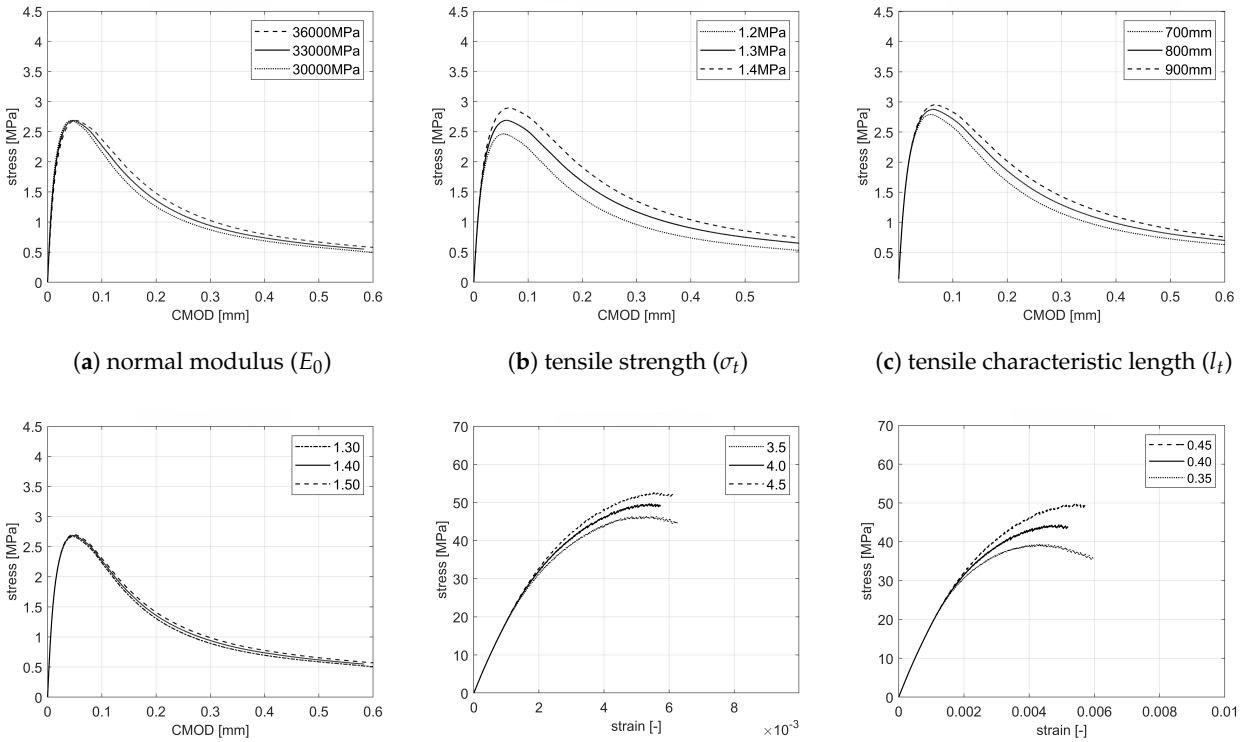
Table 5. Parameter reference values.

LDPM		LDPM-F	
Parameter	**Reference Value**	**Parameter**	**Reference Value**
E_0 (MPa)	33,000	E_f (MPa)	3900
σ_t (MPa)	1.3	σ_{uf} (MPa)	560
l_t (mm)	800	k_{rup} (-)	0.00
n_t (-)	1.40	γ_p (-)	0.00
α (-)	0.25	τ (MPa)	2.5
μ_0 (-)	0.40	β (-)	0.00
μ_∞ (-)	0.00	G_d (N/m)	0.27
σ_{N0} (MPa)	600	k_{sn} (-)	0.55
σ_{c0} (MPa)	190	$k_{sp} \cdot \sigma_t$ (MPa)	125
κ_{c0} (-)	2.00	k_{cg} (-)	2.65
κ_{c1} (-)	1.00		
κ_{c2} (-)	2.00		
E_d/E_0 (-)	1.00		
r_{st} (-)	4.00		
k_t (-)	0.00		
k_s (-)	0.00		
k_c (-)	0.00		

In the LDPM, the macroscale response of plain concrete undergoing a three-point bending test is governed by (i) the normal modulus E_0, (ii) tensile strength σ_t, (iii) the tensile characteristic length l_{cr}, and (iv) the softening exponent n_t.

In uniaxial compression, instead, a significant role is played also by (v) the shear strength ratio $r_{st} = \sigma_s/\sigma_t$, and (vi) the initial friction μ_0. The response is also heavily affected by the tensile strength σ_t, which governs the formation of the splitting cracks, which are ultimately responsible for the failure in unconfined compression. It is worth remarking that LDPM parameters refer to constitutive laws at the mesoscale: they shape

the material response along the triangular facets where the LDPM polyhedral cells interact. Therefore, the modification of a parameter governing the post-peak response in tension produces an effect whenever, along each facet, the strain exceeds the linear elastic limit. The sensitivity analysis aims to discuss the modifications detectable in the macroscale behaviour when changes on the LDPM mesoscale parameters are introduced. In Figure 3, the results for plain concrete are shown.



(**a**) normal modulus (E_0) (**b**) tensile strength (σ_t) (**c**) tensile characteristic length (l_t)

(**d**) softening exponent (n_t) (**e**) shear strength ratio (σ_s/σ_t) (**f**) initial friction (μ_0)

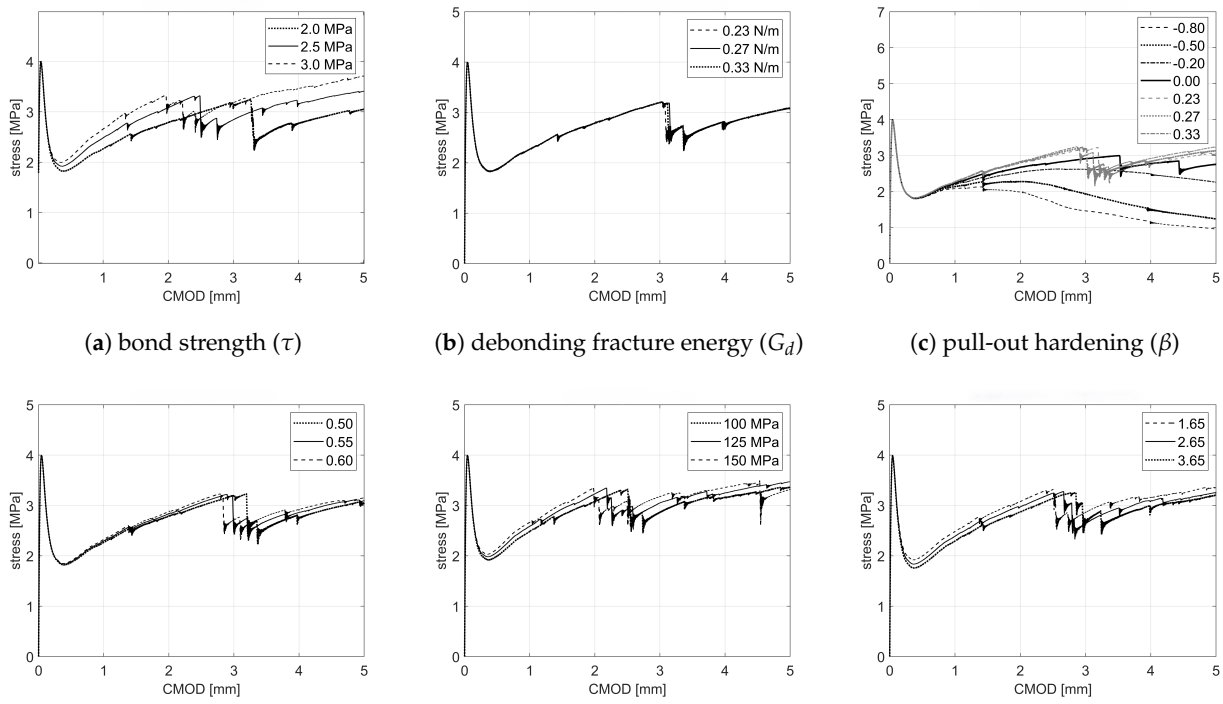
Figure 3. Sensitivity analysis for plain concrete.

The trends in Figure 3a–c comply with the definition of fracture energy at the mesoscale, $G_t = l_{cr}\sigma_t^2/2E_0$. As a matter of fact, despite the considered ranges of E_0, σ_t, and l_{cr} being similar, the effect produced by σ_t is more pronounced. The normal modulus E_0 ranges between 30 and 36 GPa (Figure 3a). The simulated macroscale response does not change significantly: the initial branches up to the peak substantially coincide, whereas the softening behaviour tends to become smoother as E_0 increases. This evidence seems to prove that a stiffer material induces a slightly better energy distribution within the fracture process zone, resulting in a higher concrete toughness. Figure 3b shows that higher concrete strength in tension shifts the peak, not only upwards, as expected, but also to the right, meaning that it is reached with higher values of CMOD. The increase in tensile characteristic length from 700 to 900 mm (+28%) yields a growth in the fracture energy (Figure 3c), though one lower than that one induced by a smaller increase in tensile strength: from 1.2 to 1.4 MPa (+16%). This complies with the above-mentioned expression of G_t. It is also worth highlighting that higher l_{ct} corresponds to higher peak stress at the macroscale. The softening exponent n_t impacts the ductility and LDPM facet transition from pure tension to pure shear responses after the peak. As n_t increases, the toughness of concrete increases accordingly, as shown in Figure 3d. The ratio of shear to tensile strength r_{st} and the initial friction μ_0 have a considerable impact on the peak in uniaxial compressive strength (Figure 3e,f). Both parameters affect the shear behaviour at the mesoscale, hence

their changes imply noticeable modifications in the response that the LDPM facets near the loading plates experience.

The sensitivity to the LDPM-F parameters governing the fibres' crack-bridging mechanism has been assessed by simulating only three-point bending tests, since this effect is much more evident when the material undergoes flexural tests.

In the LDPM-F, the fibre–matrix interaction mechanisms are governed by (i) bond strength τ, (ii) debonding fracture energy G_d, and the following four material parameters: (iii) β, which governs the pull-out hardening, (iv) k_{sn}, (v) k_{sp}, and (vi) k_{cg}, which account for snubbing, spalling and Cook–Gordon effects, respectively. In Figure 4, the results of the sensitivity analysis are shown.



(**a**) bond strength (τ) (**b**) debonding fracture energy (G_d) (**c**) pull-out hardening (β)

(**d**) snubbing parameter (k_{sn}) (**e**) spalling parameter (k_{sp}) (**f**) Cook–Gordon parameter (k_{cg})

Figure 4. Sensitivity analysis for fibre-reinforced concrete.

Figure 4a shows that the frictional resistance at the fibre–matrix interface significantly affects the post-peak behaviour. The rehardening branch following the formation of the first crack is steeper, with higher τ, whereas the second peak does not vary, being for all the investigated values equal to approximately $3.25 \div 3.35$ MPa. On the other hand, it is interesting to notice that the latter is reached for different values of CMOD. Notably, the second relevant drop in nominal stress (Equation (23)) that occurs for CMOD is inversely proportional to the bond strength. In addition, it is worth highlighting that the above-mentioned drop for lower values of τ is much more brittle, with the formation of a single major second crack, whereas as τ increases, a mechanism with multiple cracks is triggered, featuring the formation of several smaller cracks related to smaller stress drops.

During the fibre pull-out, the debonding fracture energy has a negligible impact with respect to frictional strength. Then, the macroscale response remains substantially unchanged for the different investigated values of G_d (Figure 2b). Minor modifications can be detected at the second relevant stress drop, where higher G_d values imply a slight shift rightwards. Figure 2b illustrates the effect of pull-out force hardening and softening during the single fibre pull-out, and Figure 4c shows how it affects the behaviour at the macroscale.

Differently from all the other parameters, for which three representative values have been analysed, β has been made ranging over seven different values, as it varies between -1 (softening) and +1 (hardening). When β is negative, the resistance during fibre pull-out is minimal, resulting in low FRC post-peak strength and low ductility. On the other hand, as this parameter increases towards positive values, the material exhibits a post-crack hardening behaviour with higher toughness. Figure 4d,e illustrate the effect of matrix snubbing and spalling parameters, respectively. The FRC toughness and ductility are directly proportional to both parameters, k_{sn} and k_{sp}.

Finally, Figure 4f shows that as k_{cg} gradually increases from 1.65 to 3.65, the slippage of each fibre is enlarged by an increasing value of v_{cg} (see Equation (17)), resulting in a higher fibre bridging load, and, hence, more effective multi-cracking patterns. The model is, therefore, able to capture a more ductile response.

5. LDPM and LDPM-F Calibration and Validation

5.1. Calibration Process

The proper model calibration requires the availability of experimental data relevant to fracture and uni/multiaxial compression tests. However, for the parameters considered in the sensitivity analysis, the data collectable through uniaxial compression and three-point bending tests already represent a proper basis to perform a correct calibration. The results of the experimental tests are hereinafter presented in terms of nominal stress vs. CMOD curves, for fracture tests, whereas, for compression tests, only the peak stress is considered, as the full nominal stress vs. axial displacement was not recorded.

The calibration process consists of simulating the whole test set-up, i.e., specimen geometry, topology of the measuring instruments, kinematic boundary conditions, and loading regimes, and identifying the set of model parameters that achieves agreement between simulated and experimentally determined behaviour through a trial-and-error approach. Then, it is worth highlighting that the calibration is performed by modifying the *mesoscale* governing parameters such as to reach agreement with *macroscale* behaviour. The LDPM mesh was generated by assuming the actual maximum aggregate size, $d_a = 12$ mm [75], whereas the minimum d_0 was chosen in order to have a fair compromise between accuracy and computational cost: $d_0 = d_a/2 = 6$ mm [41]. Furthermore, both the simulated stress-opening curves and the simulated compressive strength values reported in the following represent the average of six virtual experiments with different particle configurations, i.e., six different meshes. This approach minimizes the bias introduced by a specific specimen with a related particle configuration.

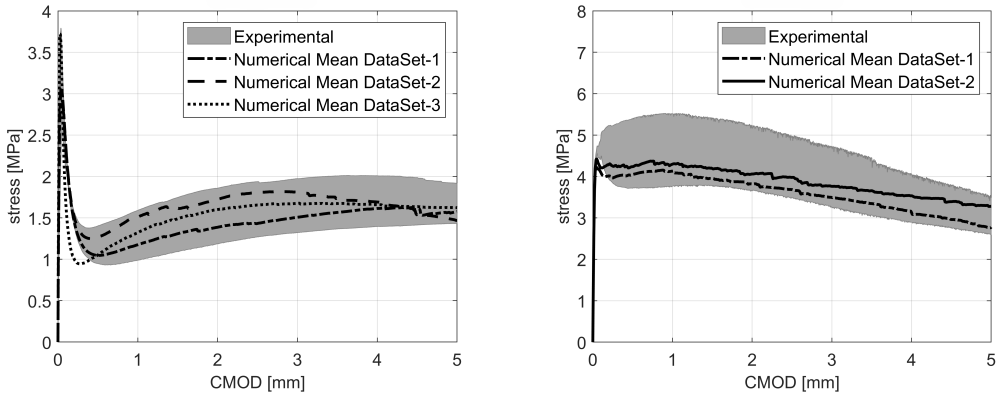
A proper calibration should focus first on the plain matrix by calibrating the mesoscale LDPM properties against three-point bending tests and unconfined compression tests without fibres. Then, once the matrix parameters are calibrated, the LDPM-F parameters can be identified, simulating the FRC. However, for the material of interest, only tests on the fibre-reinforced composite were available; hence, the calibration process of both LDPM and LDPM-F parameters was carried out jointly, introducing possible ambiguities in the selected parameters.

The lack of dedicated tests on the plain matrix may lead to unreliable LDPM parameters. Some of them might be either under- or overestimated in order to match the experimental trends detected in the fibre-reinforced composite. The main issues in cases of limited experimental data are, hence, represented by the difficulty in (i) identifying cause–effect correlations between material composition and macroscale behaviour, and (ii) distinguishing which effects are due to plain matrix properties and which others relate to either the fibres' features and/or fibre–matrix interaction. Similar problems can also arise within the LDPM calibration against test results on the plain matrix. In that case, as a matter

of fact, it might be difficult to calibrate the full set of LDPM parameters if the experimental campaign does not cover the whole range of inelastic contitutive laws implemented in the model, namely (i) fracture, (ii) compaction and pore collapse under compression, and (iii) frictional behaviour.

In order to cope with the above-mentioned ambiguities, the results of the sensitivity analysis were essential to guide the calibration process. The latter consisted of (1) identifying LDPM and LDPM-F parameters by seeking the best fitting between three-point bending experimental and numerical average outcomes, where the numerical average was computed out of the results achieved by employing six different meshes; (2) the calibrated model was then used to simulate the compression test, in order to check the compliance with the compressive strength measured in the lab; (3) in case the set of calibrated parameters did not allow us to capture the compressive strength, changes were implemented on those parameters governing the plain matrix response, assuming that fibres have a negligible effect on the behaviour in compression; (4) three-point bending tests were simulated by using the revised set of model parameters to check if the previous match still held. Steps 2 to 4 were repeated until convergence was achieved. The sensitivity analysis helped us to implement changes in the parameters in order to achieve the desired curve fitting. Since dedicated experimental evidence for the plain matrix was not available, the first tentative LDPM parameters were assumed through an educated guess, based on previous LDPM-based works dealing with materials featuring similar properties [41,42,45,50,52].

In Tables 6 and 7 and Figure 5, the comparisons between experimental and numerical results for compression and fracture tests, respectively, are shown. Notably, in Table 7, the experimental and numerical representative values for nominal flexural residual tensile strength, as defined by EN-14651, are listed in terms of average and coefficient of variation, expressed in percentages. The numerical vs. experimental comparison is shown in terms of Δ, which is defined, for the i-th parameters X_i, as $\Delta = [(X_{i.num.avg} - X_{i.exp.avg})/X_{i.exp.avg}] \times 100$. The calibration was performed for two mixes, as shown earlier in Table 2, which differ in the type and dosage of fibres: I-P5 includes 5.0 kg/m^3 of polypropylene fibres, whereas I-S30 presents 30.0 kg/m^3 of steel fibres. As a result, since the same mixing and casting operations were accomplished for their preparation, the different mechanical response between the two mixes must be attributed to the different type and dosage of fibres.



(**a**) I-P5 (**b**) I-S30

Figure 5. 3PBT nominal stress vs. CMOD curves for (**a**) I-P5 mix (PP fibres) (**b**) I-S30 mix (steel fibres): experimental vs. numerical results.

Table 6. Peak strength in uniaxial compression test [MPa]: experimental vs. numerical results.

Mix	Experimental			Numerical		
	Min	Max	Average	Avg. (Set-1)	Avg. (Set-2)	Avg. (Set-3)
I-P5	30.26	42.03	38.03	37.68	37.80	38.02
I-S30	43.32	50.83	45.39	44.99	45.06	-

Table 7. Nominal residual flexural tensile strength [MPa]: experimental vs. numerical results.

Mix		Experimental		Numerical					
				Set-1		Set-2		Set-3	
		Avg.	CoV (%)	Avg.	Δ (%)	Avg.	Δ (%)	Avg.	Δ (%)
I-P5	f_L	3.05	21.73	3.07	−1.67	3.05	−2.28	3.69	18.39
	f_{R1}	1.11	24.13	1.16	−9.76	1.53	18.60	1.33	3.13
	f_{R2}	1.32	22.93	1.39	−8.58	1.72	13.26	1.61	5.77
	f_{R3}	1.50	20.46	1.51	−8.07	1.81	10.09	1.68	2.02
	f_{R4}	1.58	18.72	1.62	−4.75	1.70	0.00	1.67	−1.68
I-S30	f_L	4.57	5.33	4.43	−1.11	4.20	−6.33	-	-
	f_{R1}	4.47	19.42	4.30	−7.38	4.09	−11.84	-	-
	f_{R2}	4.45	17.89	4.08	−7.93	3.81	−14.02	-	-
	f_{R3}	4.06	18.33	3.76	−5.66	3.50	−12.22	-	-
	f_{R4}	3.56	17.23	3.54	2.61	3.10	−10.18	-	-

The calibration process was performed by following an iterative approach. Upon reaching a match between simulated and experimentally measured responses in three-point bending tests, the same set of parameters was used to simulate the cube compression tests. When the numerical–experimental match was not confirmed in compression, the LDPM parameters must be adjusted accordingly. Once the simulated average compressive strength matched the experimental one with sufficient accuracy ($\varepsilon \leq 1\%$), the *revised* set was used to re-perform the numerical simulation of the fracturing test. If the numerical curves did not fit the experimental scatter, the parameters must be further adjusted. This iterative process continued until the numerical results from both the three-point bending and compression test complied with the experimental data for the material at hand.

One of the aims of this paper is to provide insights into the LDPM and LDPM-F calibration process. As stands out from Table 6 and Figure 5, the match between numerical outcomes and experimental data can be achieved with different sets of model parameters. In this study, for the IP-5 and I-S30 mixes, respectively, three and two datasets were identified. They are reported in Tables 8 and 9. The parameters which were not calibrated in this study were assumed based on relevant published works [41,42]: $\alpha = 0.25$, $\sigma_{c0} = 190$ MPa, $H_{c0}/E_0 = 0.4$, $k_{c0} = 2.0$, $E_d/E_0 = 1.0$, $\mu_\infty = 0.0$, $\sigma_{N0} = 600$ MPa, $\beta = 0.0$, $k_{c1} = 1.0$, $k_{c2} = 5.0$. Firstly, it is interesting to notice that all the identified sets ensure a sufficient agreement with the experimental results. For IP-5, the numerical average compressive strength values are equal to 37.68 MPa, 37.80 MPa, and 38.02 MPa for Set-1, Set-2, and Set-3, respectively, whereas the detected average experimental value is 38.03 MPa. Relevant to the fracture test, all the sets allow us to capture the macroscale material behaviour. As a matter of fact, the numerical curves in Figure 5a fit well the experimental scatter. The same result is confirmed for the I-S30 mix. Also in this case, the experimental average compressive strength (47.99 MPa) is captured with sufficient accuracy by both the sets of calibrated parameters (44.99 MPa for Set-1, 45.06 for Set-2). The good agreement between simulations and tests, regardless of the parameter set used, is further confirmed by the comparison shown in Figure 5b, in which it stands out how Set-1 and Set-2 allow us to obtain numerical results complying with the three-point bending evidence.

Table 8. LDPM calibrated parameters.

	IP-5			I-S30	
Parameter	**Set-1**	**Set-2**	**Set-3**	**Set-1**	**Set-2**
E_0 [GPa]	36.0	36.0	40.0	40.0	40.0
σ_t [MPa]	1.62	1.62	3.25	3.25	3.25
l_t [mm]	800	800	150	150	150
n_t [-]	0.2	0.2	0.2	0.2	0.2
σ_s/σ_t [-]	4.0	4.0	2.6	2.6	2.6
μ_0 [-]	0.3	0.3	0.3	0.3	0.3

Table 9. LDPM-F calibrated parameters.

	IP-5			I-S30	
Parameter	**Set-1**	**Set-2**	**Set-3**	**Set-1**	**Set-2**
$k_{sp}\sigma_t$ [MPa]	110	150	150	150	150
k_{rup} [-]	0.0	0.0	0.45	0.57	0.5
k_{sn} [-]	0.5	0.7	0.7	0.4	0.4
τ_0 [MPa]	1.72	3.0	1.75	8.0	9.5
η [-]	0.0	0.0	0.0	0.0	0.0
G_d [N/m]	0.3	5.0	5.0	5.0	5.0
β [-]	0.25	-0.25	0.01	-0.07	-0.01
k_{cg} [-]	3.6	3.6	3.6	2.0	2.0

Both experimental and numerical data reveal discrepancies in peak stress during fracture and compression tests. However, the two analysed mixes, i.e., I-P5 and I-S30, are approximately identical, despite a negligible difference in aggregate content. This result provides evidence of the influence of fibre type and volume fraction on the FRC behaviour, also under compression.

The calibration showcase highlights an important point: low-scale accurate models, such as the LDPM and LDPM-F, require a number of parameters which govern the mechanical response at the model scale, which for the LDPM is the mesoscopic one. Since the calibration relies on the comparison between experimental and numerical results at the macroscale, due to the unfeasibility of performing reliable tests at the mesoscale, the parameter identification is generally challenging. As an example, the mesoscale tensile strength σ_t simultaneously affects the macroscale response in both the considered loading regimes. On one hand, it determines significant modifications on the material toughness in bending, as discussed in Section 4, and, at the same time, it is one of the parameters governing the failure in unconfined compression, which is typically induced by the propagation of splitting cracks. Beyond the multiple correlations linking mesoscale constitutive laws and macroscale response, it is also possible that different sets of the governing parameters might result in similar simulated macroscale behaviours.

The quality of the calibration process must be assessed by proving whether the calibrated model is able to predict the response of the same material in configurations not considered for the calibration itself, without further adjustments of the governing parameters. For FRC notched prisms undergoing a three-point bending test, and hence approaching the failure through the propagation of one major crack along the ligament, an additional criterion to assess the reliability of the calibrated set might be to compare the number of fibres intersecting the crack in the numerical simulation with the experimental fibre count at the same location. The same can be done for their direction. These parameters are particularly important because they govern the post-peak behaviour. The matching between numerical and experimental curves with a substantial difference in the number of fibres intersecting the crack might mean that the calibration of the LDPM-F parameters have

been biased by the fibre distribution, leading to either an underestimation or overestimation of their contribution to the macroscopic material response.

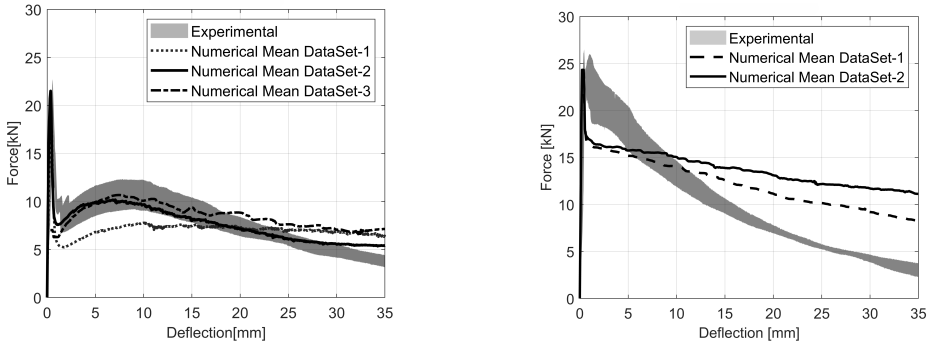
5.2. Validation Process

The validation of the LDPM's predictive capability is performed by simulating tests executed on samples or structural elements that are made from the same material but that have not been used in the calibration process. Options are varying the geometry, loading scheme and stress state, boundary conditions, etc., of course without varying the calibrated governing parameters. In this study, the identified sets of parameters for the two investigated mixes were used to simulate energy absorption tests on round panels. The objective is to verify the accuracy of the calibrated parameters and validate the behaviour of fibre-reinforced concrete under significantly different testing conditions. The deformation and crack opening ranges are much larger in the round panel test than those detectable through three-point bending, thereby providing a more comprehensive assessment. Similar to the approach followed during calibration, the average numerical curve resulting from multiple simulations with different particle configurations was compared to the experimental test outcome to ensure a robust validation process.

Figure 5a shows that three distinct parameter sets were able to capture the PPFRC flexural behaviour adequately within the experimental scatter. Nevertheless, when validating their capacity against round panel tests, Figure 6a shows that the Set-2 numerical curve exhibited a more significant pull-out softening compared to the post-peak response obtained by employing Set-1 and Set-3. The use of Set-2 led to higher simulated stress values than the other sets until the CMOD reached 4 mm, but they declined at a higher rate thereafter. The maximum peak stress is 3.7 MPa, obtained when Set-3 was used, likely due to the higher tensile strength value adopted.

In Figure 6a, it stands out that, although all the sets were demonstrated to be capable of accurately capturing the three-point bending results, only Set-2 confirmed the predictive capability that the calibrated model is expected to have. As a matter of fact, the Set-2 average numerical curve matches the experimental trend with remarkable precision. On the contrary, Set-3 was not able to capture the softening tail properly, and Set-1 did not allow us to catch the post-peak behaviour at all.

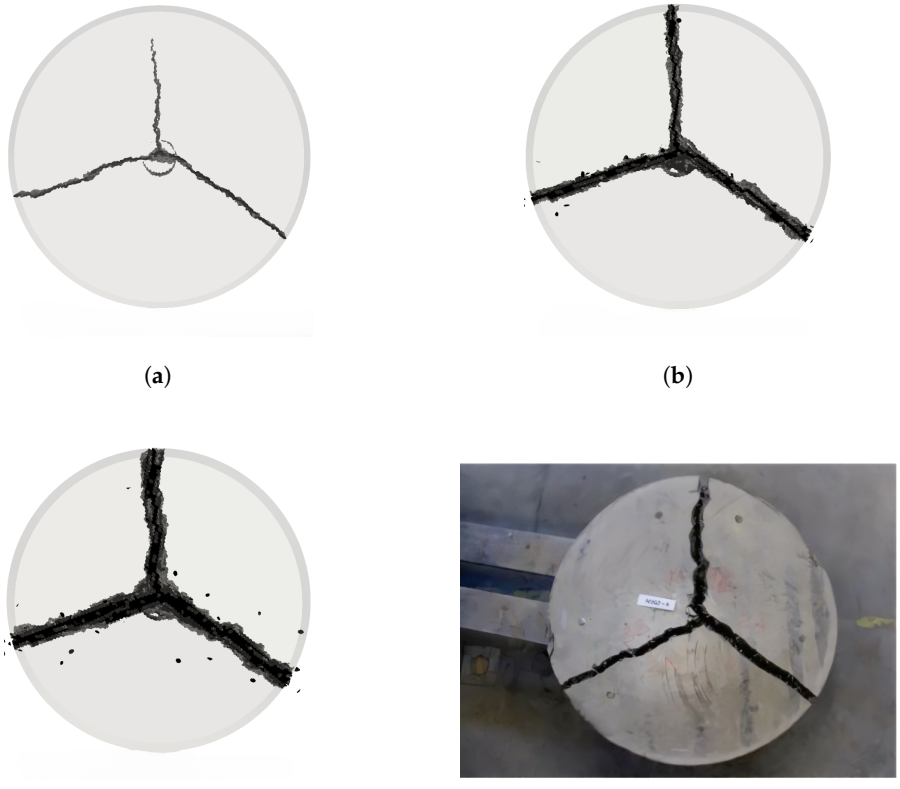
Figure 6b showcases the situation in which none of the calibrated sets yields reliable predictions. Set-1 and Set-2 seem to capture the peak stress with sufficient accuracy, but both sets miss in following the softening branch correctly. This result offers two debatable points. Firstly, the calibration might be improved in order to identify a better harmonisation among the governing parameters. Along with that, it is interesting to notice the qualitatively different post-peak behaviour detected in the round panel tests if compared to that recorded during the three-point bending test. The latter, shown in Figure 5b, proves that the material does feature a considerable ductility, with a low strength decay after the first crack formation. However, the energy absorption test on the round panel shows that the material experiences a completely different response, i.e., a significant softening after the peak, as demonstrated by the experimental scatter reported in Figure 6b. While the model captures reasonably well the response in the three-point bending test used for calibration, the predictions of the panel tests show an abrupt post-peak drop followed by slow softening, while the experiments indicate a gradual, slowly decelerating softening behaviour. The FRC with synthetic fibres instead exhibited similar behaviour in both fracturing and energy absorption tests. Therefore, it might be possible that the better predictions achieved for the PPFRC stem from the higher consistency between the responses in the two different sets of laboratory tests.



(**a**) I-P5 (**b**) I-S30

Figure 6. Validation through round panel energy absorption tests: (**a**) I-P5 mix (PP fibres), (**b**) I-S30 mix (steel fibres).

Despite the debatable results in terms of curve fitting, the calibrated model has proven to be capable of properly predicting the crack patterns induced in the round panels due to deflection (Figure 7). Figure 7a shows the initial crack that emerges on the external contact surface between the loading plate and specimen. As the deflection increases, a crack forms in the centre and propagates towards the edge of the specimen in three different directions, each approximately 120° apart. The width of the crack increases as the centre deflection increases, as shown in Figure 7b,c. This results in an increase in the specimen's total toughness due to the crack-bridging phenomenon. Additionally, Figure 7c,d illustrate the LDPM-F's capability of capturing the final experimental crack pattern numerically.



(**a**) (**b**)

(**c**) (**d**)

Figure 7. Comparison between numerical and experimental crack propagation on the bottom surface of a round panel. (**a**) Inital crack propagation. (**b**) Increment in crack width. (**c**) Final crack propagation. (**d**) Experimental round panel crack path [75].

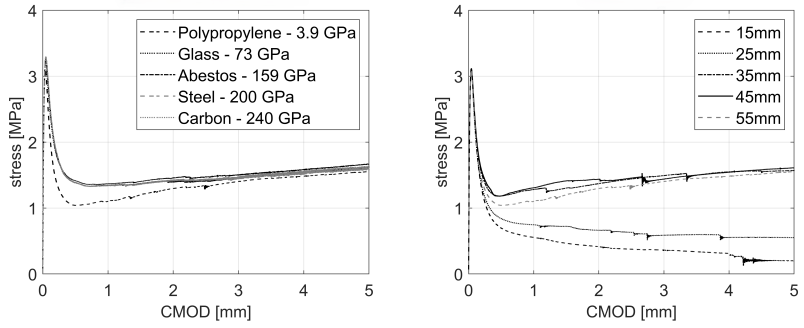
6. Parametric Study

The aim of the parametric study is to investigate how mechanical and geometrical features of the fibres might affect the macroscale response of the resulting FRC in the post-cracking stage, to eventually serve as valuable tool for a performance-oriented material optimisation. To this purpose, three-point bending tests were simulated for a reference material, which had the IP-5 mix composition (see Table 3) and Set-1 model parameters (Table 10). Then, the following fibre properties were varied over intervals representative of the products available today on the market: (i) Young's modulus, (ii) length, (iii) cross-section, and (iv) volume fraction. Originally, the fibre tensile strength was also included in the parametric study. However, none of the investigated materials reached the tensile failure along the activated fibres, and then, the resulting behaviour at the macroscale had no meaninigful differences.

Table 10. LDPM and LDPM-F parameter sets used as reference in the parametric study.

LDPM	E_0 [GPa]	σ_t [MPa]	l_t [mm]	n_t [-]	σ_s/σ_t [-]	μ_0 [-]		
	36.0	1.62	800	0.2	4.0	0.3		
LDPM-F	$k_{sp}\sigma_t$ [MPa]	k_{rup} [-]	k_{sn} [-]	τ_0 [MPa]	η [-]	G_d [N/m]	β [-]	k_{cg} [-]
	110	0.0	0.5	1.72	0.0	0.3	0.25	3.6

In Figure 8, the results of the parametric study are shown in terms of nominal stress vs. CMOD curves. The curves represent the average of six different simulations, performed on meshes featuring different spatial aggregate distributions within the specimen volume.



(**a**) fibre elastic modulus E_f (**b**) fibre length l_f

(**c**) fibre cross-section A_f (**d**) fibre volume fraction V_f

Figure 8. Parametric analysis to predict the response of FRCs featuring different types and dosages of fibres.

6.1. Young's Modulus

The transfer of forces between fibres and the concrete matrix is influenced by the fibres' Young's modulus [78]. Depending on the material, Young's modulus is typically 3.9 GPa for polypropylene fibres, 73 GPa for glass, 159 GPa for asbestos, 200 GPa for steel, and 240 GPa for carbon [75,79,80]. A higher elastic modulus results in a stiffer and stronger fibre that can better withstand the stress generated in the specimen (Figure 8a). It can be noted that the transfer of stress after concrete cracking is quicker in glass than in polypropylene fibres due to its higher elastic modulus. The toughness of FRC increases as the fibre elastic modulus goes from 3.9 GPa to 73 GPa. However, in order to observe appreciable variations in toughness, the elastic modulus has to vary at least by one or more orders of magnitude. It is worth stressing that in these simulations, only the Young's modulus was varied, while the fibre cross-section and other material properties were kept constant. Naturally, in reality also, the tensile strength changes accordingly when different fibre materials are considered.

6.2. Length

The length of macro-fibres ranges from 38 to 50 mm, whereas micro-fibres are typically measured between 12 and 38 mm [81]. In this study, the investigated fibre lengths are 15, 25, 35, 45, and 55 mm. In Figure 8b, the numerical results are shown. The number of fibres in the specimen decreases when fibre length increases for the same volume fraction. For micro-fibres, an increase in fibre length corresponds to a higher flexural toughness. This may be attributed to the shorter frictional length during pull-out despite a greater number of activated fibres. The rate of flexural toughness's increase from 25 to 35 mm is higher than from 15 to 25 mm. Furthermore, with macro-fibres, the difference in the flexural toughness for 35 and 45 mm is subtle; however, a reduction in flexural toughness is observed with the 55 mm fibre length. This is due to a lower number of fibres for the same volume fraction. The optimum fibre length for the same volume fraction ranges between 35 and 45 mm for the investigated parameter combination.

6.3. Cross-Section

In order to investigate the effect of cross-section on the fibre crack-bridging potential and, in turn, on the macroscale response, the following values were considered: 0.25 mm^2, 0.45 mm^2, and 0.65 mm^2. Similar to the previous section, when a constant fibre length and volume fraction are applied, the overall number of fibres generated decreases as the fibre cross-sectional area increases. The fibre activated in the crack bridging is lower for fibres with a higher cross-sectional area. Figure 8c indicates the decrease in flexural toughness of FRC as the fibre sectional area is increased from 0.25 mm^2 to 0.45 mm^2. Similarly, a further decrease in flexural toughness is observed as the fibre cross-sectional area is increased from 0.45 mm^2 to 0.65 mm^2 due to a lower number of fibres intersecting the induced cracks.

6.4. Volume Fraction

The dosage of fibres significantly affects the FRC's post-peak strength. The given IP-5 mix used includes polypropylene fibres with a density of 1000 kg/m^3. For fibre dosages of 5, 7, and 10 kg/m^3, the corresponding volume fractions are 0.005, 0.007, and 0.010, respectively. Unsurprisingly, for a given cross-section and length, as the fibre dosage increases, the numbers of placed and activated fibres (i.e., intersecting a crack) rise. As a consequence, the flexural toughness of the material grows accordingly (Figure 8d). At the same time, a larger volume of fibres leads to the formation of a larger number of (micro)cracks during the fracture process. Looking at Figure 8, it stands out that, for a given target response, these three parameters should be optimised consistently.

7. Conclusions

In this paper, the extended version of the LDPM used to incorporate the effect of fibre in concrete, the LDPM-F, was used to numerically capture the experimental behaviour of two fibre-reinforced concretes under short-term loading conditions. The LDPM and LDPM-F parameters were calibrated, for the mixes of interest, against the experimental data collected through three-point bending and uniaxial compression tests. As a result of the calibration process, multiple parameter sets were identified for each mix, in order to showcase potential ambiguities resulting from calibrations to actually insufficient experimental data. The quality of the different candidate calibrations was then assessed in the validation stage. The latter consisted of simulating the same materials subjected to different testing conditions: energy absorption tests on round panels. Along with that, the model sensitivity was evaluated with respect to the changes in the governing parameters relevant to the tests used as a reference. Finally, a numerical parametric study was conducted in order to show the model's potential to be used as a valuable tool in the process of application-oriented optimisation of material mix design.

Based on the numerical results, the comparison with the experimental evidence, and the trends identified in both the sensitivity analysis and parametric study, it is possible to draw the following conclusions:

- The simulated response in three-point bending at the macroscale is mainly affected by the mesoscale fracture energy G_t, hence by normal modulus E_0, tensile characteristic length l_{ct}, and tensile strength σ_t. The latter is the parameter which has shown the highest impact on peak stress and material toughness. The parameters most relevant to compressive strength at the macroscale are the initial friction coefficient μ_0, and mesoscale tensile and shear strengths, σ_t and σ_s, respectively, where the latter is expressed in the LDPM as function of the tensile strength by means of the parameter r_{st}, which is the shear-to-tensile strength ratio.
- As expected, the LDPM-F parameters govern the post-cracking behaviour. The sensitivity analysis has shown that the fibre–matrix bond strength τ and the pull-out hardening coefficient β are the two parameters having the most significant effects on the simulated macroscale response to bending. Notably, they control (i) the number of cracks forming after the peak is reached, and, as a consequence, (ii) whether the material experiences either softening or hardening in the post-peak branch. The parameters relevant to the micromechanical interaction between the fibre and the surrounding matrix do have an impact, but not one as crucial as τ and β.
- The LDPM and LDPM-F are able to accurately capture the experimental trends detected through three-point bending tests on notched prisms and uniaxial compression tests on cubes.
- For the mixes adopted as study cases, only three-point bending tests and unconfined compression tests on fibre-reinforced concrete with one fibre content were available. Due to the lack of a sufficiently rich experimental dataset, no unique parameter set could be obtained during the inverse calibration process. This clearly demonstrates the need for more experimental data and clean validation to assess the quality of the calibration and ensure reliable predictions.
- The validation stage has shown that only one of the identified sets, for the FRC with polypropylene fibres, was able to accurately match the experimental trends recorded for round panels undergoing energy absorption tests, while the other sets resulted only in acceptable predictions.
- For the FRC with steel fibres, instead, none of the calibrated sets was able to match the experimental results. However, this might be related to differences in the post-cracking behaviour observed in the laboratory during three-point bending and energy

absorption tests. The former show substantial hardening and a ductile response, whereas the panels show significant softening after cracking initiation.

In the last decade, LDPM-based models have been developed to simulate multiphysics phenomena and capture the response of ordinary and advanced cementitious materials for a wide variety of civil engineering applications. This paper aims to provide some insights into the calibration of LDPM-Fs and their validation for fibre-reinforced concrete, which ultimately may allow numerical LDPM simulations to be used, either to optimise the design of the mixture composition, or to identify the most appropriate testing procedure to experimentally characterise a new cement-based material. In this perspective, both sensitivity analyses and parametric studies might provide some guidance for future research, in spite of the inescapable complexity due to the large number of model parameters paired with typically limited experimental data. The latter surely represents a burden to deal with when the LDPM is adopted to simulate the behaviour of concrete. However, the significantly demanding calibration is largely rewarded by the superior capabilities, provided by the LDPM over recent decades, to capture experimental trends in a wide range of structural applications. They refer to (i) durability issues (e.g., chloride diffusion in undamaged, cracked, and healed conditions), (ii) purely mechanical applications (e.g., strength and stiffness build-up from casting onwards, tertiary creep), and (iii) multiphysics scenarios (e.g., response to fire exposure, shrinkage).

Author Contributions: Conceptualization, R.W.-W., C.M. and N.B.; methodology, R.W.-W., C.M. and N.B.; software, R.W.-W.; validation, A.C. and R.W.-W.; formal analysis, S.P. and A.C.; investigation, S.P. and C.D.P.; resources, R.W.-W., C.M. and N.B.; data curation, S.P., A.C. and C.D.P.; writing—original draft preparation, S.P. and A.C.; writing—review and editing, A.C., R.W.-W., C.M. and N.B.; visualization, S.P. and A.C.; supervision, R.W.-W., C.M. and N.B.; project administration, R.W.-W., C.M. and N.B.; funding acquisition, R.W.-W., C.M. and N.B. All authors have read and agreed to the published version of the manuscript.

Funding: This research received no external funding

Data Availability Statement: Data are contained within the article.

Acknowledgments: The numerical analyses were performed by means of MARS, an explicit dynamic code distributed by ES3 Inc. (Engineering and Software System Solutions), which is gratefully acknowledged.

Conflicts of Interest: The authors declare no conflicts of interest.

References

1. Ahmad, J.; Zhou, Z. Mechanical Properties of Natural as well as Synthetic Fiber Reinforced Concrete: A Review. *Constr. Build. Mater.* **2022**, *333*, 127353. [CrossRef]
2. Blazy, J.; Blazy, R. Polypropylene fiber reinforced concrete and its application in creating architectural forms of public spaces. *Case Stud. Constr. Mater.* **2021**, *14*, e00549. [CrossRef]
3. Zhang, P.; Wang, C.; Gao, Z.; Wang, F. A review on fracture properties of steel fiber reinforced concrete. *J. Build. Eng.* **2023**, *67*, 105975. [CrossRef]
4. Yuan, Z.; Jia, Y. Mechanical properties and microstructure of glass fiber and polypropylene fiber reinforced concrete: An experimental study. *Constr. Build. Mater.* **2021**, *266*, 121048. [CrossRef]
5. Kang, M.C.; Yoo, D.Y.; Gupta, R. Machine learning-based prediction for compressive and flexural strengths of steel fiber-reinforced concrete. *Constr. Build. Mater.* **2021**, *266*, 121117. [CrossRef]
6. Ahmad, J.; Majdi, A.; Al-Fakih, A.; Deifalla, A.; Althoey, F.; El Ouni, M.; El-Shorbagy, M. Mechanical and Durability Performance of Coconut Fiber Reinforced Concrete: A State-of-the-Art Review. *Materials* **2022**, *15*, 3601. [CrossRef]
7. Manfredi, R.P.; de Andrade Silva, F. Test Methods for the Characterization of Polypropylene Fiber Reinforced Concrete: A Comparative Analysis. *KSCE J. Civ. Eng.* **2020**, *24*, 856–866. [CrossRef]
8. Hughes, B.; Fattuhi, N. Stress-strain curves for fibre reinforced concrete in compression. *Cem. Concr. Res.* **1977**, *7*, 173–183. [CrossRef]

9. Lee, S.C.; Oh, J.H.; Cho, J.Y. Compressive Behavior of Fiber-Reinforced Concrete with End-Hooked Steel Fibers. *Materials* **2015**, *8*, 1442–1458. [CrossRef] [PubMed]
10. Hassan, A.; Jones, S.; Mahmud, G. Experimental test methods to determine the uniaxial tensile and compressive behaviour of ultra high performance fibre reinforced concrete (UHPFRC). *Constr. Build. Mater.* **2012**, *37*, 874–882. [CrossRef]
11. Monazami, M.; Gupta, R. Investigation of mechanical behavior and fracture energy of fiber-reinforced concrete beams and panels. *Cem. Concr. Compos.* **2022**, *133*, 104656. [CrossRef]
12. Xu, L.; Wang, S.; Li, B.; Huang, L.; Chi, Y. An elastoplastic damage constitutive model for hybrid steel-polypropylene fiber reinforced concrete. *Int. J. Damage Mech.* **2022**, *31*, 1506–1532. [CrossRef]
13. Zhang, J.; Wu, Z.; Yu, H.; Ma, H.; Da, B. Mesoscopic Modeling Approach and Application for Steel Fiber Reinforced Concrete under Dynamic Loading: A Review. *Engineering* **2022**, *16*, 220–238. [CrossRef]
14. Fayed, A.; Sherbini, A.; Abou El-Mal, H. Mixed mode fracture behavior of fiber reinforced concrete; Experimental and numerical analysis adopting cracked Brazilian disc specimen. *Ain Shams Eng. J.* **2023**, *14*, 102132. [CrossRef]
15. Wang, X.; Fan, F.; Lai, J.; Xie, Y. Steel fiber reinforced concrete: A review of its material properties and usage in tunnel lining. *Structures* **2021**, *34*, 1080–1098. [CrossRef]
16. Huang, Y.; Huang, J.; Zhang, W.; Liu, X. Experimental and numerical study of hooked-end steel fiber-reinforced concrete based on the meso- and macro-models. *Compos. Struct.* **2023**, *309*, 116750. [CrossRef]
17. Zia, A.; Ali, M. Behavior of fiber reinforced concrete for controlling the rate of cracking in canal-lining. *Constr. Build. Mater.* **2017**, *155*, 726–739. [CrossRef]
18. Buratti, N.; Mazzotti, C.; Savoia, M. Post-cracking behaviour of steel and macro-synthetic fibre-reinforced concretes. *Constr. Build. Mater.* **2011**, *25*, 2713–2722. [CrossRef]
19. Soulioti, D.V.; Barkoula, N.M.; Paipetis, A.; Matikas, T.E. Effects of Fibre Geometry and Volume Fraction on the Flexural Behaviour of Steel-Fibre Reinforced Concrete. *Strain* **2011**, *47*, e535–e541. [CrossRef]
20. Holschemacher, K.; Mueller, T.; Ribakov, Y. Effect of steel fibres on mechanical properties of high-strength concrete. *Mater. Des. 1980–2015* **2010**, *31*, 2604–2615. [CrossRef]
21. Khan, M.; Fuzail Hashmi, A.; Shariq, M.; Ibrahim, S. Effects of incorporating fibres on mechanical properties of fibre-reinforced concrete: A review. *Mater. Today Proc.* 2023, *in press* . [CrossRef]
22. Roelfstra, P.; Sadouki, H.; Wittmann, F. Le béton numérique. *Mater. Struct.* **1985**, *18*, 327–335. [CrossRef]
23. Caballero, A.; Carol, I.; López, C. A meso-level approach to the 3D numerical analysis of cracking and fracture of concrete materials. *Fatigue Fract. Eng. Mater. Struct.* **2006**, *29*, 979–991. [CrossRef]
24. Caballero, A.; López, C.; Carol, I. 3D meso-structural analysis of concrete specimens under uniaxial tension. *Comput. Methods Appl. Mech. Eng.* **2006**, *195*, 7182–7195. [CrossRef]
25. Caballero, A.; Carol, I.; López, C. New results in 3d meso-mechanical analysis of concrete specimens using interface elements. In *Computational Modelling of Concrete Structures*; CRC Press: Boca Raton, FL, USA, 2020; pp. 43–52.
26. Schlangen, E.; van Mier, J. Simple lattice model for numerical simulation of fracture of concrete materials and structures. *Mater. Struct.* **1992**, *25*, 534–542. [CrossRef]
27. Bolander, J.E.; Saito, S. Fracture analyses using spring networks with random geometry. *Eng. Fract. Mech.* **1998**, *61*, 569–591. [CrossRef]
28. Yip, M.; Li, Z.; Liao, B.S.; Bolander, J.E. Irregular lattice models of fracture of multiphase particulate materials. *Int. J. Fract.* **2006**, *140*, 113–124. [CrossRef]
29. Nagai, K.; Sato, Y.; Ueda, T. Mesoscopic Simulation of Failure of Mortar and Concrete by 2D RBSM. *J. Adv. Concr. Technol.* **2004**, *2*, 359–374. [CrossRef]
30. Jin, C.; Buratti, N.; Stacchini, M.; Savoia, M.; Cusatis, G. Lattice discrete particle modeling of fiber reinforced concrete: Experiments and simulations. *Eur. J. Mech.-A Solids* **2016**, *57*, 85–107. [CrossRef]
31. Fanella, D.; Krajcinovic, D. Continuum Damage Mechanics of Fiber Reinforced Concrete. *J. Eng. Mech.* **1985**, *111*, 995–1009. [CrossRef]
32. Li, F.; Li, Z. Continuum damage mechanics based modeling of fiber reinforced concrete in tension. *Int. J. Solids Struct.* **2001**, *38*, 777–793. [CrossRef]
33. Peng, X.; Meyer, C. A continuum damage mechanics model for concrete reinforced with randomly distributed short fibers. *Comput. Struct.* **2000**, *78*, 505–515. [CrossRef]
34. Xu, Z.; Hao, H.; Li, H. Mesoscale modelling of fibre reinforced concrete material under compressive impact loading. *Constr. Build. Mater.* **2012**, *26*, 274–288. [CrossRef]
35. Xu, Z.; Hao, H.; Li, H. Mesoscale modelling of dynamic tensile behaviour of fibre reinforced concrete with spiral fibres. *Cem. Concr. Res.* **2012**, *42*, 1475–1493. [CrossRef]
36. Fang, Q.; Zhang, J. Three-dimensional modelling of steel fiber reinforced concrete material under intense dynamic loading. *Constr. Build. Mater.* **2013**, *44*, 118–132. [CrossRef]

37. Han, T.S.; Feenstra, P.H.; Billington, S.L. Simulation of Highly Ductile Fiber-Reinforced Cement-Based Composite Components Under Cyclic Loading. *ACI Struct. J.* **2003**, *100*, 749 – 757.
38. Caner, F.C.; Bažant, Z.P.; Wendner, R. Microplane model M7f for fiber reinforced concrete. *Eng. Fract. Mech.* **2013**, *105*, 41–57. [CrossRef]
39. Oliver, J.; Mora, D.; Huespe, A.; Weyler, R. A micromorphic model for steel fiber reinforced concrete. *Int. J. Solids Struct.* **2012**, *49*, 2990–3007. [CrossRef] [PubMed]
40. Cusatis, G.; Pelessone, D.; Mencarelli, A. Lattice Discrete Particle Model (LDPM) for failure behavior of concrete. I: Theory. *Cem. Concr. Compos.* **2011**, *33*, 881–890. [CrossRef]
41. Cusatis, G.; Mencarelli, A.; Pelessone, D.; Baylot, J. Lattice Discrete Particle Model (LDPM) for failure behavior of concrete. II: Calibration and validation. *Cem. Concr. Compos.* **2011**, *33*, 891–905. [CrossRef]
42. Del Prete, C.; Boumakis, I.; Wan-Wendner, R.; Vorel, J.; Buratti, N.; Mazzotti, C. A lattice discrete particle model to simulate the viscoelastic behaviour of macro—Synthetic fibre reinforced concrete. *Constr. Build. Mater.* **2021**, *295*, 123630. [CrossRef]
43. Alnaggar, M.; Bhanot, N. A machine learning approach for the identification of the Lattice Discrete Particle Model parameters. *Eng. Fract. Mech.* **2018**, *197*, 160–175. [CrossRef]
44. Schauffert, E.A.; Cusatis, G. Lattice Discrete Particle Model for Fiber-Reinforced Concrete. I: Theory. *J. Eng. Mech.* **2012**, *138*, 826–833. [CrossRef]
45. Schauffert, E.A.; Cusatis, G.; Pelessone, D.; O'Daniel, J.L.; Baylot, J.T. Lattice Discrete Particle Model for Fiber-Reinforced Concrete. II: Tensile Fracture and Multiaxial Loading Behavior. *J. Eng. Mech.* **2012**, *138*, 834–841. [CrossRef]
46. Sagar, R.V.; Saha, I.; Basu, D.J.; Kundu, T. Statistics of acoustic emission waveforms in characterizing the fracture process zone in fibre-reinforced cementitious materials under mode I fracture. *Struct. Health Monit.* **2024**, *23*, 2083–2101. [CrossRef]
47. Mpalaskas, A.C.; Kytinou, V.K.; Zapris, A.G.; Matikas, T.E. Optimizing Building Rehabilitation through Nondestructive Evaluation of Fire-Damaged Steel-Fiber-Reinforced Concrete. *Sensors* **2024**, *24*, 5668. [CrossRef]
48. Smith, J.; Cusatis, G.; Pelessone, D.; O'Daniel, J.; Baylot, J. *Calibration and Validation of the Lattice Discrete Particle Model for Ultra High-Performance Fiber-Reinforced Concrete*; Asce Library: Lawrence, KS, USA, 2012; pp. 394–405.
49. Smith, J.; Cusatis, G.; Pelessone, D.; Landis, E.; O'Daniel, J.; Baylot, J. Discrete modeling of ultra-high-performance concrete with application to projectile penetration. *Int. J. Impact Eng.* **2014**, *65*, 13–32. [CrossRef]
50. Smith, J.; Cusatis, G. Numerical analysis of projectile penetration and perforation of plain and fiber reinforced concrete slabs. *Int. J. Numer. Anal. Methods Geomech.* **2017**, *41*, 315–337. [CrossRef]
51. Shen, L.; Luzio, G.D.; Zhu, D.; Yao, X.; Cusatis, G.; Cao, M.; Han, Y.; Wang, Y.; Ren, Q. Mechanical Responses of Steel Fiber–Reinforced Concrete after Exposure to High Temperature: Experiments and Mesoscale Discrete Modeling. *J. Eng. Mech.* **2021**, *147*, 04021084, [CrossRef]
52. Cibelli, A.; Ferrara, L.; Di Luzio, G. Multiscale and multiphysics discrete model of self-healing of matrix and interfacial cracks in fibre reinforced cementitious composites: Formulation, implementation and preliminary results. *Cem. Concr. Compos.* **2024**, *148*, 105465. [CrossRef]
53. Boumakis, I.; Marcon, M.; Ninčević, K.; Czernuschka, L.M.; Wan-Wendner, R. Concrete creep and shrinkage effect in adhesive anchors subjected to sustained loads. *Eng. Struct.* **2018**, *175*, 790–805. [CrossRef]
54. Cibelli, A.; Pathirage, M.; Cusatis, G.; Ferrara, L.; Di Luzio, G. A discrete numerical model for the effects of crack healing on the behaviour of ordinary plain concrete: Implementation, calibration, and validation. *Eng. Fract. Mech.* **2022**, *263*, 108266. [CrossRef]
55. Cibelli, A.; Di Luzio, G.; Ferrara, L. Numerical simulation of the chloride penetration in cracked and healed UHPC via a discrete multiphysics model. *J. Eng. Mech.* **2023**, *149*, 05023001. [CrossRef]
56. Alnaggar, M.; Di Luzio, G.; Cusatis, G. Modeling Time-Dependent Behavior of Concrete Affected by Alkali Silica Reaction in Variable Environmental Conditions. *Materials* **2017**, *10*, 471. [CrossRef] [PubMed]
57. Yang, L.; Pathirage, M.; Su, H.; Alnaggar, M.; Di Luzio, G.; Cusatis, G. Computational modeling of temperature and relative humidity effects on concrete expansion due to alkali–silica reaction. *Cem. Concr. Compos.* **2021**, *124*, 104237. [CrossRef]
58. Wan, L.; Wendner, R.; Liang, B.; Cusatis, G. Analysis of the behavior of ultra high performance concrete at early age. *Cem. Concr. Compos.* **2016**, *74*, 120–135. [CrossRef]
59. Cibelli, A.; Ferrara, L.; Di Luzio, G. A combined numerical and experimental study on the mechanical aging of high slag content High Performance Concrete. *J. Build. Eng.* **2024**, *98*, 111294. [CrossRef]
60. Zhang, Y.; Di Luzio, G.; Alnaggar, M. Coupled multi-physics simulation of chloride diffusion in saturated and unsaturated concrete. *Constr. Build. Mater.* **2021**, *292*, 123394. [CrossRef]
61. Cibelli, A.; Wan-Wendner, R.; Di Luzio, G.; Nigro, E. Multiphysics-Lattice Discrete Particle Model: Possible strategies for upscaling. *Procedia Struct. Integr.* **2024**, *64*, 183–190. [CrossRef]
62. Cusatis, G.; Bažant, Z.P.; Cedolin, L. Confinement-Shear Lattice Model for Concrete Damage in Tension and Compression: I. Theory. *J. Eng. Mech.* **2003**, *129*, 1439–1448. [CrossRef]

63. Cusatis, G.; Bažant, Z.P.; Cedolin, L. Confinement-Shear Lattice Model for Concrete Damage in Tension and Compression: II. Computation and Validation. *J. Eng. Mech.-Asce* **2003**, *129*, 1449–1458. [CrossRef]
64. Cusatis, G.; Bažant, Z.P.; Cedolin, L. Confinement-shear lattice CSL model for fracture propagation in concrete. *Comput. Methods Appl. Mech. Eng.* **2006**, *195*, 7154–7171. [CrossRef]
65. Pelessone, D. *Discrete Particle Method*; Technical report; Engineering and Software System Solutions, Inc.: San Diego, CA, USA, 2005.
66. Hang, S. TetGen, a Delaunay-based quality tetrahedral mesh generator. *ACM Trans. Math. Softw* **2015**, *41*, 11.
67. Lin, Z.; Kanda, T.; Li, V. On interface characterizationand performance of fiber-reinforced cementitious composites. *J. Concr. Sci. Eng.* **1999**, *1*, 173–184.
68. Lin, Z.; Li, V.C. Crack bridging in fiber reinforced cementitious composites with slip-hardening interfaces. *J. Mech. Phys. Solids* **1997**, *45*, 763–787. [CrossRef]
69. Yang, E.H.; Wang, S.; Yang, Y.; Li, V.C. Fiber-Bridging Constitutive Law of Engineered Cementitious Composites. *J. Adv. Concr. Technol.* **2008**, *6*, 181–193. [CrossRef]
70. Li, V.; Wang, Y.; Backer, S. Effect of inclining angle, bundling and surface treatment on synthetic fibre pull-out from a cement matrix. *Composites* **1990**, *21*, 132–140. [CrossRef]
71. Cook, J.; Gordon, J.E. A mechanism for the control of crack propagation in all-brittle systems. *Proc. R. Soc. London. Ser. A Math. Phys. Sci.* **1964**, *282*, 508–520.
72. Li, V.C.; Stang, H.; Krenchel, H. Micromechanics of crack bridging in fibre-reinforced concrete. *Mater. Struct.* **1993**, *26*, 486–494. [CrossRef]
73. Kanda, T.; Li, V.C. Interface Property and Apparent Strength of High-Strength Hydrophilic Fiber in Cement Matrix. *J. Mater. Civ. Eng.* **1998**, *10*, 5–13. [CrossRef]
74. Press, W.H.; Teukolsky, S.A.; Vetterling, W.T.; Flannery, B.P. *Numerical Recipes in Fortran 90: Numerical Recipes in Fortran 77v. 2. Numerical Recipes in Fortran 90*; Cambridge University Press: Cambridge, UK, 1992.
75. Buratti, N.; Incerti, A.; Tilocca, A.; Mazzotti, C.; Paparella, M.; Draconte, M. Energy absorption tests on fibre-reinforced-shotcrete round and square panels. In *Tunnels and Underground Cities: Engineering and Innovation Meet Archaeology, Architecture and Art*; CRC Press: Boca Raton, FL, USA, 2019; pp. 1842–1851.
76. *EN 12390-5:2019*; Testing Hardened Concrete. Part 5: Flexural Strength of Test Specimens; European Committee for Standardization (CEN): Brussels, Belgium, 2019.
77. Marangi, P. Computational Modeling of Fiber Reinforced Concrete with Application to Projectile Penetration. Ph.D. Thesis, University of Bologna, Bologna, Italy, 2010.
78. Del Prete, C.; Wan-Wendner, R.; Buratti, N.; Mazzotti, C. *Parametric Study of the Lattice Discrete Particle Model (LDPM) Constitutive Law for Fiber Reinforced Concretes (FRCs)*; CRC Press: Boca Raton, FL, USA, 2022; pp. 525–532.
79. Ramujee, K. Strength properties of polypropylene fiber reinforced concrete. *Int. J. Innov. Res. Sci. Eng. Technol.* **2013**, *2*, 3409–3413.
80. Yao, W.; Li, J.; Wu, K. Mechanical properties of hybrid fiber-reinforced concrete at low fiber volume fraction. *Cem. Concr. Res.* **2003**, *33*, 27–30. [CrossRef]
81. Del Prete, C. Experimental and Numerical Investigation on Short and Long Term Performance of Macro-Synthetic Fibre Reinforced Concrete Materials. Ph.D. Thesis, University of Bologna, Bologna, Italy, 2020. [CrossRef]

Disclaimer/Publisher's Note: The statements, opinions and data contained in all publications are solely those of the individual author(s) and contributor(s) and not of MDPI and/or the editor(s). MDPI and/or the editor(s) disclaim responsibility for any injury to people or property resulting from any ideas, methods, instructions or products referred to in the content.